



A computational approach for phase-field model of quasi-brittle fracture under dynamic loading

Roman Vodička

Received: 24 April 2024 / Accepted: 12 July 2024
© The Author(s) 2024

Abstract A computational model is formulated for studying dynamic crack propagation in quasi-brittle materials exposed to time-dependent loading conditions. Under such conditions, inertial effects of structural components play an important role in modelling crack propagation problems. The computational model is proposed within the theory of regularised cracks which uses a damage-like internal variable. Here, fracture considers phase-field damage which gives rise to a material degradation in a narrow material strip defining the regularised crack. Based on the energy formulation using the Lagrangian of the system, the proposed computational approach introduces a staggered scheme adopted to solve the coupled system and providing it in a variational form within the time stepping procedure. The numerical data are obtained by quadratic programming algorithms implemented together with a finite element code.

Keywords Phase-field fracture · Quadratic programming · Dynamic crack propagation · Staggered approach · Mixed fracture mode

1 Introduction

The ideas which are important in solid mechanics include phenomena like damage, degradation and ultimately fracture. In many situations, a quasi-static consideration of those processes is sufficient to provide satisfactorily accurate data which agree with real behaviour of structures. Nevertheless, when the processes are fast or structures are substantially large, the inertial effect may considerably modify also the mechanical response of such structures or of their components and subsequently change cracks and their formation processes, too. One of the crucial items here is a finite speed of transferring any information, including crack propagation. Therefore, complex computational models of fracture really account for dynamic crack propagation.

The cracks are modelled in two basic ways in calculations: discretely or continuously. The former assumes the crack as a discontinuity in geometry as it is seen macroscopically, while the latter diffuses the discontinuity into the material by making it degraded, as it appears in its micro-structure, and relates the degradation to changes in physical characteristics. These changes are called damage and computationally they are represented by additional internal variables (Frémond 1985; Maugin 2015). Such a concept led also to Phase-Field Models (PFM), where the damaged material appears in narrow material bands called regularised cracks.

R. Vodička (✉)
Faculty of Civil Engineering, Technical University of
Košice, Vysokoškolská 4, 04200 Košice, Slovakia
e-mail: roman.vodicka@tuke.sk

Many brittle fracture computational approaches, ultimately appropriate for computational power of finite-element implementations, are based on the variational fracture model, proposed in [Francfort and Marigo \(1998\)](#), [Bourdin et al. \(2000\)](#) accounting for minimisation of energy in a solid through analysis of strain energy in domains and surface energy of arisen cracks related to Griffith's concept of fracture. The original concept was later modified in many ways to establish it within the concept of regularised cracks. Initially showing the relation to the discrete concept of cracks by mathematical tools of Γ convergence, see [Dal Maso \(2012\)](#), which gave birth to the phase-field approach as brought forth in [Bourdin et al. \(2008\)](#). The computational power of the developed approach provided robust computational PFM implementations with a rigorous thermodynamical background in [Miehe et al. \(2010\)](#), [Del Piero \(2013\)](#), [Molnár and Gravouil \(2017\)](#). There appeared many improvements and modifications of the phase-field methods for fracture from that time. Such adjustments specified distinct issues of the approach related to the characteristics of the computational model: scale parameter related to the width of the regularised crack, degradation function describing the damage process of the material ([Kuhn et al. 2015](#); [Sargado et al. 2018](#)), its effect on fracture in various materials ([Fang et al. 2022](#); [Freddi and Mingazzi 2022](#); [Raj and Murali 2020](#); [Xu et al. 2022](#)), crack nucleation conditions and related processes ([Tanné et al. 2018](#); [Wu 2017](#); [Yin and Zhang 2019](#); [Wang et al. 2020](#)) etc. The variety of degradation functions used by many researcher is interpreted by particular material behaviour, properties of the computational approach and many times they are supported by empirical results. In addition, many computational procedures distinguish between cracking mechanisms in distinct crack modes, revealing different amount of energy, used in variationally based techniques, which is needed to initiate and propagate cracks in various crack modes, see [Zhang et al. \(2017\)](#), [Feng and Li \(2022\)](#). Hence, the applications of the phase-field model appeared in calculation combining loading in tension, compression, or shear ([Cao et al. 2022](#); [Luo et al. 2022](#); [Yue et al. 2022](#)). Generally, all such modifications assisted to overcome limitation of the original Griffith theory.

As mentioned in the beginning, it is also significant to stress those efforts which implemented the influence of inertia within the present fracture concept. With PFM seen as an energy based method, a

similar energy formulation is a good strategy to be utilised. Therefore, the dynamic fracture concepts use the Lagrangian for introducing kinetic energy into fracture mechanics approaches as done by [Borden et al. \(2012\)](#), [Zhang et al. \(2021\)](#), [Weinberg and Wieners \(2022\)](#) and intensively studied under various conditions as documented e. g. by [Li et al. \(2023\)](#), [Zeng et al. \(2023\)](#), [Zhang et al. \(2023\)](#), [Peng et al. \(2023\)](#). Naturally, the solution is constructed on the Hamilton variational principle extended to systems with dissipation, here naturally represented by unidirectionality of crack propagation processes ([Kružík and Roubíček 2019](#); [Roubíček and Panagiotopoulos 2017](#)). Additionally, the speed of the processes in the materials can also be affected by their rheological properties. It is natural to consider and to sum them up to the dissipative effects of the models of fracture. They complete the physical properties of the analysed systems and also make improvements in numerical treatment of the computational solution. Thus, it is useful to consider fracture models with a visco-elastic rheology pertinent to solid materials ([Roubíček 2020](#)).

The main objective of the paper is to provide an upgrade of the author's works ([Vodička 2022, 2023](#)) for quasi-static mixed-mode PFM fracture propagation by a novel computational approach where inertia is considered for nucleation and propagation of cracks. This upgraded approach is also performed here and assessed by a computer code implementing PFM for solids, see also [Vodička \(2024\)](#). The main contributions of the study are: (i) a full energy expressed computational formulation for dynamically evolving fracture in terms of PFM damage; (ii) specifically introduced terms for energy dissipation motivated by fracture mode-mixity and by a general four parametric solid rheology; (iii) a variationally based computational approach implemented in an in-house MATLAB Finite Element Method (FEM) computer code for testing various problems with crack propagation under time dependent loads. The algorithms are verified in various structural elements exposed to various types of loading and made of damageable visco-elastic materials. The tested solids represent typical academic examples, though in some cases simulating real experimental observations obtained by other authors.

The rest of the contribution is organized as follows. PFM is formulated in terms of strain, fracture, kinetic and dissipated energies stressing the mixed mode character of fracture in Sect. 2. The details of the computa-

tional implementation of the approach are provided in Sect. 3, focusing on the illustrating the time discretisation as a tool which provides variational methodology for the evolution process, and schematic computational details of FEM approximation in relation to applied methods of mathematical programming. Examples of computations are shown in Sect. 4. The calculations validate the discussed aspects of the dynamic model for fracture, and the dependence of the cracking phenomena on some material characteristics in the structure under load. Finally, Sect. 5 provides concluding remarks.

2 Description of the computational model

The changes in force and deformation quantities representing interaction of a solid structural body with surrounding can be expressed in terms of energy, let simplify the situation to 2D case under plane strain conditions. Consider the body, denoted Ω , bounded by a contour Γ , see Fig. 1, to be elastic with stiffness tensor C . Such an isotropic material requires for introducing C two parameters: presently, (plain strain) bulk modulus K_p and shear modulus μ are used. Changes in loads applied to bodies may also dissipate energy, which is to be considered for time dependent loadings. Therefore, also a rheological description for the material is implemented introducing viscosity tensor D . For a simplification of notation, the rheological properties of the material are related to the elastic ones through a relaxation time parameter τ_r . A four parametric solid material presented in Kružík and Roubíček (2019) is used for a complete description of visco-elastic material behaviour. The scheme of this rheology is also shown in Fig. 1, where the generic elastic stiffness is denoted C_i , $i = 1, 2$ and the generic damper characteristic is D_i , so that $D_i = \tau_{ri}C_i$. The stress–strain relation corresponding to the scheme is described by the relations $\sigma = C_1(e(u) - e_2) + D_1\dot{e}(u)$, $C_1(e(u) - e_2) = C_2e_2 + D_2\dot{e}_2$, where σ denotes stress, e is strain pertaining to the displacement u , e_2 is a part of the strain as seen in Fig. 1, and ‘dot’ means the derivative with respect to time t . For the material used in the model, it is written as

$$\sigma = C \left(\left(1 + \frac{1}{\gamma} \right) (e(u) - e_2) + \tau_{r1} \dot{e}(u) \right),$$

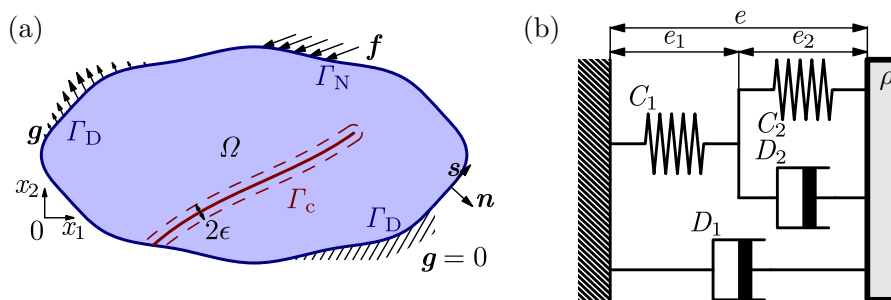
$$\left(1 + \frac{1}{\gamma} \right) (e(u) - e_2) = (1 + \gamma)e_2 + \tau_{r2} \dot{e}_2, \quad (1)$$

where e introduces the small strain tensor $e = e(u) = \frac{1}{2}(\nabla u + (\nabla u)^T)$ (u is the displacement field), and σ is the stress tensor. Thus the four parameters include stiffness (K_p or μ), stiffness ratio γ (chosen such that without dampers $\gamma = \frac{C_2}{C_1}$), and two time relaxation parameters τ_{ri} . This four parametric solid model may be reduced to simpler solid rheologies. If $\tau_{r1} = 0$, the rheology is referred to as Poynting-Thomson, if $\tau_{r2} = 0$ the rheology may be simplified to Kelvin-Voigt model. Additionally, the stiffness parameters may use different triples for the rest characteristics in order to catch different behaviour of the volumetric and shear waves propagating through the medium. Anyhow, the rheology introduces an internal variable which pertains to a part of strain denoted e_2 , it is also used to complete the trajectory of the solution.

The boundary Γ is split into two non-overlapping parts Γ_D^B and Γ_N^B according to prescribed Dirichlet and Neumann boundary conditions, respectively. It means that along the Γ_D^B part the displacement field u is given by a time dependent function $u(t) = g(t)$, which includes constraints and loads controlled by displacements. Surface tractions p are controlled by applied forces $p(t) = \sigma \cdot n = f(t)$ on the Γ_N^B part, with n being the outward unit normal vector. This part naturally involves also the load-free boundary. Demonstratively, the boundary conditions are shown in Fig. 1.

The picture also includes another curve formed inside the body—the actual crack, it is denoted Γ_c in Fig. 1. Such macroscopic crack is usually a result of changes in microscopic structure of the material. In many computational models, the formation of micro-faults is interpreted as a degradation of the material, therefore also forming of the crack is simulated by a degradation process. This degradation is determined by another internal variable α which has a damage-like character: α at any point of the body and at any instant takes values in the range $[0; 1]$ and degradation is a process which starts with $\alpha = 0$ pertaining to the intact material, and terminates with appearing of a crack represented by the value $\alpha = 1$. When describing the trajectory of the solution, it necessary involves also this variable, whose distribution in the body simulates a crack. As a continuous distribution of the variable is supposed, because there is a transition band from intact state to actual crack as represented by the width ϵ of such a band in Fig. 1, the crack model is usually referred to as regularised.

Fig. 1 Description of the deformable body (a), a smear crack characteristic, boundary conditions and constraints, with a scheme of the rheological model (b)



Summarising, the complete trajectory requires solution of three variables to be found in a time range $t \in [0; T]$: the displacement field \mathbf{u} and two internal variables of partial strain \mathbf{e}_2 and of damage α .

In fracture mechanics, a crack formation process can be identified by a release of energy proportional to the size of the crack. Pertinent energy in a Griffith-like model is expressed by an integral $\int_{\Gamma_c} G_c \, d\Gamma$, which introduces the fracture energy G_c as a crack characteristic. It may be constant but also may depend on other physical variables as temperature or speed of crack propagation. Below, the model is equipped by the dependence on deformation state to adjust crack-mode sensitivity. Nevertheless, the integration domain Γ_c , it means the extension of the crack at the instant t , is not known a priori, as long as the crack develops according to the loading history.

The dynamic evolution in the structural body will be described using energy principles. First, the stored energy is considered. It includes strain energy of the visco-elastic solid and the energy accumulated due to crack forming process as mentioned above. The representation of the latter may be introduced by the aforementioned internal parameter α available at each point of the material domain. The replacement of the integral along Γ_c can be obtained by a regularisation functional, (Ambrosio and Tortorelli 1990), which makes displacements continuous across a crack and provides models of smeared cracks called phase field models. There exist several such regularisations, one introduced in Tanné et al. (2018) presents the energy equivalent to that of the cracks in the form: $\int_{\Omega} \frac{3}{8} G_c^I \left(\frac{1}{\epsilon} \alpha + \epsilon (\nabla \alpha)^2 \right) \, d\Omega$, which is evaluated in whole known body Ω , unlike the standard crack Γ_c , which is unknown. Simultaneously, the elastic material properties (here, K_p and μ) progressively decrease according to a predefined degradation function Φ such that for cracks (maximal damage) they vanish. They

are required to obey the relations $\Phi(0) = 1$, $\Phi(1) = \delta$, ($0 < \delta \ll 1$ to guarantee positiveness of the strain energy in the case of a crack), $\Phi'(x) < 0$ for all $x \in [0; 1]$ (for computational purposes also $\Phi'(1) = 0$ and $\Phi''(x) > 0$). The result is the regularised crack, with no discontinuity and only a narrow band of degraded material inside a band of a finite width determined by ϵ . Generally, as can be also checked by the aforementioned form of the regularised energy of fracture, small value of ϵ does not allow α to move from the initial (usually intact) state by the first term in the integrand, and allows high (but still finite) gradients due to the second term. Let us also mention that the length parameter ϵ can be used to control a stress criterion in damage and crack propagation, see Tanné et al. (2018), Sargado et al. (2018), Vodička (2023). The assumptions made about cracks expressed by the phase field variable and strain energy of the four parametric rheology model provide the stored energy at the time instant t as follows:

$$\begin{aligned} \mathfrak{E}(t; \mathbf{u}, \mathbf{e}_2, \alpha) = & \int_{\Omega} \left(\Phi(\alpha) \left(K_p |\text{sph}^+(\mathbf{e}(\mathbf{u}) - \mathbf{e}_2)|^2 \right. \right. \\ & \left. \left. + \mu |\text{dev}(\mathbf{e}(\mathbf{u}) - \mathbf{e}_2)|^2 \right) \right. \\ & \left. + K_p |\text{sph}^-(\mathbf{e}(\mathbf{u}) - \mathbf{e}_2)|^2 \right) \left(1 + \frac{1}{\gamma} \right) \\ & + \left(\Phi(\alpha) \left(K_p |\text{sph}^+ \mathbf{e}_2|^2 + \mu |\text{dev} \mathbf{e}_2|^2 \right) \right. \\ & \left. + K_p |\text{sph}^- \mathbf{e}_2|^2 \right) (1 + \gamma) \\ & + \frac{3}{8} G_c^I \left(\frac{1}{\epsilon} \alpha + \epsilon (\nabla \alpha)^2 \right) \, d\Omega. \end{aligned} \quad (2)$$

The expression is valid for admissible displacement field and phase field damage, which obey the constraints

$$\mathbf{u}|_{\Gamma_D} = \mathbf{g}(t), \quad 0 \leq \alpha \leq 1, \quad (3)$$

otherwise it is considered infinite. The energy functional also features an orthogonal split of the strain ten-

sor to spherical and deviatoric parts, i.e. $\mathbf{e} = \text{sph } \mathbf{e} + \text{dev } \mathbf{e}$, to distinguish between volumetric strain energy and shear strain energy, and their different velocity of

strain energies may be used to characterise the mode dependence. The expression for the mode dependence, given by a function $G_c(\mathbf{u}, \mathbf{e}_2)$, may thus result in a form as follows

$$G_c(\mathbf{u}, \mathbf{e}_2) = \frac{K_p \left(|\text{sph}^+(\mathbf{e}(\mathbf{u}) - \mathbf{e}_2)|^2 + \gamma |\text{sph}^+ \mathbf{e}_2|^2 \right) + \mu \left(|\text{dev}(\mathbf{e}(\mathbf{u}) - \mathbf{e}_2)|^2 + \gamma |\text{dev } \mathbf{e}_2|^2 \right)}{\frac{K_p \left(|\text{sph}^+(\mathbf{e}(\mathbf{u}) - \mathbf{e}_2)|^2 + \gamma |\text{sph}^+ \mathbf{e}_2|^2 \right)}{G_c^I} + \frac{\mu \left(|\text{dev}(\mathbf{e}(\mathbf{u}) - \mathbf{e}_2)|^2 + \gamma |\text{dev } \mathbf{e}_2|^2 \right)}{G_c^{II}}} \tag{6}$$

wave propagation. Such a split is also capable of defining material degradation related to volumetric or shear strain independently. The spherical part is additionally split to tensile and compressive parts, using the notation $v^\pm = \max(0, \pm v)$, in the sense that there is no crack opening and no damaging related to compression.

Another ingredient to the energy balance is the energy of the external forces, here, represented by the nonconservative boundary forces \mathbf{f}

$$\mathfrak{F}(t; \mathbf{u}) = \int_{\Gamma_N} \mathbf{f}(t) \cdot \mathbf{u} \, d\Gamma. \tag{4}$$

As long as the loading causes non-negligible inertial effects, the kinetic energy is also a vital part of the energy balance. The standard form is given by the relation

$$\mathfrak{K}(\dot{\mathbf{u}}) = \int_{\Omega} \frac{1}{2} \rho |\dot{\mathbf{u}}|^2 \, d\Omega, \tag{5}$$

where ρ denotes mass density of the material.

The evolution is naturally affected by processes which dissipate energy. As mentioned in the beginning, one part of the dissipation is caused by the implemented rheology of the material, as illustrated by the dampers in the scheme presented in Fig. 1 (the values of the parameters D_i in the figure are pertinently $\tau_{ri} K_p$ or $\tau_{ri} \mu$). Second, if the crack evolution is affected by other than opening mode [Mode I, cf. using the superscript I in the fracture energy in Eq. (2)], there may appear another nonlinear behaviour which dissipates additional energy. In this sense it shares a similar idea of e.g. Feng and Li (2022) and extends other like Wu (2017), Tanné et al. (2018). Here, the nonlinearity can be simulated by defining the fracture energy as mode dependent, see e.g. Benzeggagh and Kenane (1996). In particular, the model assumes it to depend on the deformation at time instant t represented here by displacement field and internal strain variable. As long as the aforementioned orthogonal split of the strain tensor separates opening from the shear, the corresponding

It can be seen that for an opening crack $G_c(\mathbf{u}, \mathbf{e}_2)$ reduces to G_c^I , and there remains just G_c^{II} in the case of the Mode II crack (shear). Additionally, the crack propagation is considered as a unidirectional process, in which α does not decrease in time. All these assumptions can be indicated by a dissipation pseudo-potential

$$\begin{aligned} \mathfrak{R}(\mathbf{u}, \mathbf{e}_2, \alpha; \dot{\mathbf{u}}, \dot{\mathbf{e}}_2, \dot{\alpha}) &= \int_{\Omega} \widehat{\Phi}(\alpha) \\ &\left(\tau_{r1} K_p |\text{sph } \mathbf{e}(\dot{\mathbf{u}})|^2 + \tau_{r2} K_p |\text{sph } \dot{\mathbf{e}}_2|^2 \right. \\ &\left. + \tau_{r1} \mu |\text{dev } \mathbf{e}(\dot{\mathbf{u}})|^2 + \tau_{r2} \mu |\text{dev } \dot{\mathbf{e}}_2|^2 \right) \\ &+ \frac{3}{8\epsilon} \left(G_c(\mathbf{u}, \mathbf{e}_2) - G_c^I \right) \dot{\alpha}^\eta \, d\Omega, \end{aligned} \tag{7}$$

provided that the constraint $\dot{\alpha} \geq 0$ in Ω is satisfied, otherwise its value is infinite. The degradation function in the viscous part is chosen in accordance with (Roubíček 2020) as $\widehat{\Phi}(\alpha) = \phi_0 + \Phi(\alpha)$ for a fixed value ϕ_0 . Observe that additional dissipation due to the crack appears only in other than opening mode. The last term vanishes and no additional energy is dissipated in opening. In the shear mode it, e.g., adds some dissipated energy if $G_c^{II} - G_c^I$ is positive.

If the solid body is evolved in time due to time dependent external loading and phenomena related to inertia are taken into account, the solution of the problem considering a general linear solid rheology and crack formation processes can be obtained from the Hamilton variational principle extended to dissipative systems, see Bedford (1985), Kružík and Roubíček (2019), as long as the used rheology and fracture dissipates mechanical energy. The principle says that the action \mathfrak{S} of the system:

$$\begin{aligned} \mathfrak{S}(\mathbf{u}, \mathbf{e}_2, \alpha) &= \int_0^T \left(\mathfrak{K}(\dot{\mathbf{u}}) - \mathfrak{E}(t; \mathbf{u}, \mathbf{e}_2, \alpha) + \mathfrak{F}(t; \mathbf{u}) \right) \\ &- \left(\int_{\Omega} \left(\mathfrak{R}'_{\dot{\mathbf{u}}} \cdot \dot{\mathbf{u}} + \mathfrak{R}'_{\dot{\mathbf{e}}_2} \cdot \dot{\mathbf{e}}_2 + \partial_{\dot{\alpha}} \mathfrak{R} \cdot \dot{\alpha} \right) \, d\Omega \right) \, dt, \end{aligned} \tag{8}$$

calculated over the fixed time interval $[0, T]$ during which the system evolves, is stationary with respect

to the trajectory $(\mathbf{u}, \mathbf{e}_2, \alpha)$ pertinent to the interval $t \in [0, T]$. The energy trinomial in the first parentheses of Eq. (8) introduces the Lagrangian. In the second parentheses, the triple $(\mathfrak{R}'_{\dot{\mathbf{u}}}, \mathfrak{R}'_{\dot{\mathbf{e}}_2}, \partial_{\dot{\alpha}}\mathfrak{R})$ defines non-conservative dissipative forces as dissipation is also defined by a (pseudo-)potential from Eq. (7). The prime denotes (Gateaux) differential (with respect to the subscript variable), and ∂ denotes the partial subdifferential (\mathfrak{R} may jump for zero damage rates $\dot{\alpha}$ due to unidirectionality of degradation process).

The Euler-Lagrange stationarity conditions provide the equation of motion and the flow rules for internal variables (strain and phase-field damage) which also introduce competition between dissipation due to viscosity and due to fracture. The relations are expressed as a system of nonlinear equations and inclusion with initial conditions in the following form

$$\begin{aligned} \mathfrak{K}'(\ddot{\mathbf{u}}) + \mathfrak{E}'_{\mathbf{u}}(t; \mathbf{u}, \mathbf{e}_2, \alpha) + \mathfrak{R}'_{\dot{\mathbf{u}}}(\mathbf{u}, \mathbf{e}_2, \alpha; \dot{\mathbf{u}}, \dot{\mathbf{e}}_2, \dot{\alpha}) \\ = \mathfrak{F}'(t; \mathbf{u}), \mathbf{u}(0, \cdot) = \mathbf{u}_0, \dot{\mathbf{u}}(0, \cdot) = \mathbf{v}_0, \\ \mathfrak{E}'_{\mathbf{e}_2}(t; \mathbf{u}, \mathbf{e}_2, \alpha) + \mathfrak{R}'_{\dot{\mathbf{e}}_2}(\mathbf{u}, \mathbf{e}_2, \alpha; \dot{\mathbf{u}}, \dot{\mathbf{e}}_2, \dot{\alpha}) = 0, \\ \mathbf{e}_2(0, \cdot) = \mathbf{e}_{20}, \\ \partial_{\alpha}\mathfrak{E}(t; \mathbf{u}, \mathbf{e}_2, \alpha) + \partial_{\dot{\alpha}}\mathfrak{R}(\mathbf{u}, \mathbf{e}_2, \alpha; \dot{\mathbf{u}}, \dot{\mathbf{e}}_2, \dot{\alpha}) \ni 0, \\ \alpha(0, \cdot) = \alpha_0. \end{aligned} \tag{9}$$

It is also supposed that the stored energy functional \mathfrak{E} is separately convex with respect to the couple $(\mathbf{u}, \mathbf{e}_2)$ and α . The initial value for the phase-field parameter usually pertains to a non-degraded state, i. e. $\alpha_0 = 0$. It is also to be mentioned that due to internal strain variable \mathbf{e}_2 , it requires an initial condition itself or through the initial stress $\boldsymbol{\sigma}_0$, as $\mathbf{e}_{20} = \mathbf{e}(\mathbf{u}_0) - \frac{\gamma}{1+\gamma}(\mathbf{C}^{-1}\boldsymbol{\sigma}_0 - \tau_{r1}\mathbf{e}(v_0))$.

As a physical reasonability of the governing relation, the system should satisfy the energy balance. Anyhow, correct interpretation of time derivative requires time independent displacement boundary condition. Thus, it is necessary to make a shift of the solution in order to separate the time dependence from the dependence on the displacement \mathbf{u} , which constrained by Eq. (3). The shift is $\mathbf{u} = \tilde{\mathbf{u}} + \tilde{\mathbf{g}}(t)$, where $\tilde{\mathbf{g}}(t)$ is a sufficiently smooth function in Ω satisfying the boundary condition on Γ_D . The new variable $\tilde{\mathbf{u}}$ then satisfies a vanishing boundary condition, which does not depend on time. The stored energy functional \mathfrak{E} of Eq. (2) is reformulated according to this separation as $\mathfrak{E}(t; \mathbf{u}, \mathbf{e}_2, \alpha) = \tilde{\mathfrak{E}}(\tilde{\mathbf{g}}(t); \tilde{\mathbf{u}}, \mathbf{e}_2, \alpha)$.

Let the relations in Eq. (9) be multiplied in the respective order by $\tilde{\mathbf{u}}, \dot{\mathbf{e}}_2, \dot{\alpha}$, integrated over the space domain (though not fully mathematically correctly due

to present discontinuities, e.g. in \mathfrak{R} with respect to damage rate $\dot{\alpha}$), and summed up. It renders

$$\begin{aligned} \int_{\Omega} (\tilde{\mathfrak{E}}'_{\mathbf{u}}(\tilde{\mathbf{g}}(t); \tilde{\mathbf{u}}, \mathbf{e}_2, \alpha) \cdot \dot{\tilde{\mathbf{u}}} + \tilde{\mathfrak{E}}'_{\mathbf{e}_2}(\tilde{\mathbf{g}}(t); \tilde{\mathbf{u}}, \mathbf{e}_2, \alpha) \cdot \dot{\mathbf{e}}_2 \\ + \partial_{\dot{\alpha}}\tilde{\mathfrak{E}}(\tilde{\mathbf{g}}(t); \tilde{\mathbf{u}}, \mathbf{e}_2, \alpha) \cdot \dot{\alpha}) d\Omega \\ + \int_{\Omega} \mathfrak{K}'(\ddot{\mathbf{u}}) \cdot \dot{\tilde{\mathbf{u}}} d\Omega + \int_{\Omega} (\mathfrak{R}'_{\dot{\mathbf{u}}}(\mathbf{u}, \mathbf{e}_2, \alpha; \dot{\mathbf{u}}, \dot{\mathbf{e}}_2, \dot{\alpha}) \cdot \dot{\tilde{\mathbf{u}}} \\ + \mathfrak{R}'_{\dot{\mathbf{e}}_2}(\mathbf{u}, \mathbf{e}_2, \alpha; \dot{\mathbf{u}}, \dot{\mathbf{e}}_2, \dot{\alpha}) \cdot \dot{\mathbf{e}}_2 \\ + \partial_{\dot{\alpha}}\mathfrak{R}(\mathbf{u}, \mathbf{e}_2, \alpha; \dot{\mathbf{u}}, \dot{\mathbf{e}}_2, \dot{\alpha}) \cdot \dot{\alpha}) d\Omega - \mathfrak{F}(t; \tilde{\mathbf{u}}) = 0. \end{aligned} \tag{10}$$

The integrand in the first term can be arranged due to $\mathfrak{K}'(\ddot{\mathbf{u}}) \cdot \dot{\mathbf{u}} = \rho \ddot{\mathbf{u}} \cdot \dot{\mathbf{u}} = \frac{d}{dt}(\frac{1}{2}\rho|\dot{\mathbf{u}}|^2)$. The second integral can be expressed as $\frac{d\tilde{\mathfrak{E}}}{dt} - \int_{\Omega} \tilde{\mathfrak{E}}'_g(\tilde{\mathbf{g}}(t); \tilde{\mathbf{u}}, \mathbf{e}_2, \alpha) \cdot \dot{\tilde{\mathbf{g}}}(t) d\Omega$ and the integral containing \mathfrak{R} can be written due to its homogeneity (i.e. its homogeneity in the rate variables $\mathfrak{R}(\cdot, \cdot, \cdot; p\dot{\mathbf{u}}, p\dot{\mathbf{e}}_2, q\dot{\alpha}) = p^2q\mathfrak{R}(\cdot, \cdot, \cdot; \dot{\mathbf{u}}, \dot{\mathbf{e}}_2, \dot{\alpha})$ for any p , and any $q > 0$) as $2\mathfrak{R}(\cdot, \cdot, \cdot; \dot{\mathbf{u}}, \dot{\mathbf{e}}_2, 0) + \mathfrak{R}(\cdot, \cdot, \cdot; 0, 0, \dot{\alpha}) - \int_{\Omega} \mathfrak{R}'_{\dot{\mathbf{u}}}(\cdot, \cdot, \cdot; \dot{\mathbf{u}}, \dot{\mathbf{e}}_2, \dot{\alpha}) \cdot \dot{\tilde{\mathbf{g}}}(t) d\Omega$, where the first two terms express the dissipation rate. Integrating it over the interval $[0; T]$ [starting from the initial conditions in Eq. (9)] provides

$$\begin{aligned} \mathfrak{K}(\dot{\mathbf{u}}(T)) - \mathfrak{K}(\dot{\mathbf{u}}(0)) + \tilde{\mathfrak{E}}(\tilde{\mathbf{g}}(T); \tilde{\mathbf{u}}(T), \mathbf{e}_2(T), \alpha(T)) \\ - \tilde{\mathfrak{E}}(\tilde{\mathbf{g}}(0); \tilde{\mathbf{u}}(0), \mathbf{e}_{20}, \alpha_0) \\ - \int_0^T \int_{\Omega} \tilde{\mathfrak{E}}'_g(\tilde{\mathbf{g}}(t); \tilde{\mathbf{u}}, \mathbf{e}_2, \alpha) \cdot \dot{\tilde{\mathbf{g}}}(t) \\ + \mathfrak{R}'_{\dot{\mathbf{u}}}(\mathbf{u}, \mathbf{e}_2, \alpha; \dot{\mathbf{u}}, \dot{\mathbf{e}}_2, \dot{\alpha}) \cdot \dot{\tilde{\mathbf{g}}}(t) + \rho \ddot{\mathbf{u}} \cdot \dot{\tilde{\mathbf{g}}} d\Omega dt \\ + \int_0^T 2\mathfrak{R}(\mathbf{u}, \mathbf{e}_2, \alpha; \dot{\mathbf{u}}, \dot{\mathbf{e}}_2, 0) \\ + \mathfrak{R}(\mathbf{u}, \mathbf{e}_2, \alpha; 0, 0, \dot{\alpha}) dt - \int_0^T \mathfrak{F}(t; \tilde{\mathbf{u}}) dt = 0. \end{aligned} \tag{11}$$

Returning back to the displacements \mathbf{u} , the energy balance is obtained:

$$\begin{aligned} \mathfrak{K}(\dot{\mathbf{u}}(T)) + \mathfrak{E}(T; \mathbf{u}(T), \mathbf{e}_2(T), \alpha(T)) \\ + \int_0^T 2\mathfrak{R}(\mathbf{u}, \mathbf{e}_2, \alpha; \dot{\mathbf{u}}, \dot{\mathbf{e}}_2, 0) \\ + \mathfrak{R}(\mathbf{u}, \mathbf{e}_2, \alpha; 0, 0, \dot{\alpha}) dt \\ = \mathfrak{K}(\dot{\mathbf{u}}(0)) + \mathfrak{E}(0; \mathbf{u}_0, \mathbf{e}_{20}, \alpha_0) \\ + \int_0^T \mathfrak{F}(t; \dot{\mathbf{u}} - \dot{\tilde{\mathbf{g}}}(t)) dt \\ + \int_0^T \int_{\Omega} (\tilde{\mathfrak{E}}'_g(\tilde{\mathbf{g}}(t); \dot{\mathbf{u}} - \dot{\tilde{\mathbf{g}}}(t), \mathbf{e}_2, \alpha) \end{aligned}$$

$$+\mathfrak{R}'_u(\mathbf{u}, \mathbf{e}_2, \alpha; \dot{\mathbf{u}}, \dot{\mathbf{e}}_2, \dot{\alpha}) + \rho \ddot{\mathbf{u}}) \cdot \tilde{\mathbf{g}}(t) d\Omega dt \quad (12)$$

read as: the kinetic energy plus stored energy of the system at time T plus energy dissipated during the time interval $[0, T]$ is equal to the kinetic energy plus stored energy of the system at time 0 plus energy due to the work of external forces at the same time range represented here by the external forces determining the functional \mathfrak{F} , and the hard-device loading prescribed by function $\mathbf{g}(t)$ at the boundary Γ_D . The dissipation that appears here is in the sense of definition of the functional \mathfrak{R} in Eq. (7) positive which guarantees thermodynamical consistency and satisfaction of the second law of thermodynamics.

Finally, the system (9) of differential relations is of the second order with respect to t due to the inertial term. In computations, it is sometimes useful to reduce it to a first order system if numerical attenuation is to be eliminated. Therefore, the variable of velocity as an independent variable is introduced by putting $\mathbf{v} = \dot{\mathbf{u}}$. The system is then modified as follows:

$$\begin{aligned} \dot{\mathbf{u}} &= \mathbf{v}, \\ \mathfrak{R}'(\dot{\mathbf{v}}) + \mathfrak{E}'_u(t; \mathbf{u}, \mathbf{e}_2, \alpha) + \mathfrak{R}'_v(\mathbf{u}, \mathbf{e}_2, \alpha; \mathbf{v}, \dot{\mathbf{e}}_2, 0) &= \mathfrak{F}'(t; \mathbf{u}), \\ \mathfrak{E}'_{e_2}(t; \mathbf{u}, \mathbf{e}_2, \alpha) + \mathfrak{R}'_{\dot{e}_2}(\mathbf{u}, \mathbf{e}_2, \alpha; \mathbf{v}, \dot{\mathbf{e}}_2, 0) &= 0, \\ \partial_\alpha \mathfrak{E}(t; \mathbf{u}, \mathbf{e}_2, \alpha) + \partial_{\dot{\alpha}} \mathfrak{R}(\mathbf{u}, \mathbf{e}_2, \alpha; 0, 0, \dot{\alpha}) &\ni 0, \end{aligned}$$

The numerical approach below will use this modified system.

3 Numerical solution and computer implementation

The computational approach for solving the evolution introduced in Eq. (13) is described in this section. The solution of the problem with respect to time using a time stepping procedure is discussed first separately from the spatial discretisation by FEM and the solution by (sequential) quadratic programming within each time step.

3.1 Time discretisation

For defining the time stepping algorithm, first notice the structure of the functional \mathfrak{E} introduced by Eq. (2). If it is viewed with respect to deformation variables, it remains convex, i.e. $\mathfrak{E}(t; \cdot, \cdot, \alpha)$ is convex at each

instant t and constant α . Similarly, convexity with respect to the phase-field variable of the restricted functional $\mathfrak{E}(t; \mathbf{u}, \mathbf{e}_2, \cdot)$ is observed while, according to the assumption, the degradation function Φ is convex. Accordingly, the functional \mathfrak{R} introduced by Eq. (7) is considered in view of the aforementioned homogeneity. This separation of variables can be maintained by using a staggered computational scheme for the time discretisation, which within each time step solves the problem separately with respect to deformation and damage quantities.

Additionally, as proposed in Roubíček and Panagiotopoulos (2017), the time stepping scheme for the first order (in time derivatives) system (13) may be implemented by means of the Crank-Nicolson formula (Crank and Nicolson 1947), which does not incorporate numerical attenuation, and thus, there remains only physical one caused by the proposed rheological model. It can also be seen as a particular choice of a general group of methods where the commonly used

$$\begin{aligned} \mathbf{u}(0, \cdot) &= \mathbf{u}_0, \\ \mathbf{v}(0, \cdot) &= \mathbf{v}_0, \\ \mathbf{e}_2(0, \cdot) &= \mathbf{e}_{20}, \\ \alpha(0, \cdot) &= \alpha_0. \end{aligned} \quad (13)$$

Newmark method belongs, see Hilber et al. (1977). Having in mind these two aspects of the computational approach, it can be noted that both use a mid-point calculation.

Now, consider time stepping with a fixed time step size τ defined by the instants $t^k = k\tau$ for $k = 1, \dots, \lceil \frac{T}{\tau} \rceil$ at which the trajectory is evaluated. At the instant t^k , it is expressed by the quadruplet $(\mathbf{u}_\tau^k, \mathbf{v}_\tau^k, \mathbf{e}_{2\tau}^k, \alpha_\tau^k)$. If \mathbf{w} generically denotes any of the variables $\mathbf{u}, \mathbf{v}, \mathbf{e}_2$, or α , the mid-point values for the time discretisation scheme are defined as $\mathbf{w}_\tau^{k-\frac{1}{2}} = \frac{\mathbf{w}_\tau^k + \mathbf{w}_\tau^{k-1}}{2}$, and the rates of the variables $\dot{\mathbf{w}}$ are approximated by the backward finite difference, e.g. $\dot{\mathbf{w}} \approx \frac{\mathbf{w}_\tau^k - \mathbf{w}_\tau^{k-1}}{\tau}$. Thus, the relations from Eq. (13) are written for all selected time instants starting from the initial conditions $\mathbf{u}_\tau^0 = \mathbf{u}_0, \mathbf{v}_\tau^0 = \mathbf{v}_0, \mathbf{e}_{2\tau}^0 = \mathbf{e}_{20}, \alpha_\tau^0 = \alpha_0$ to obtain

$$\begin{aligned} \frac{\mathbf{u}_\tau^k - \mathbf{u}_\tau^{k-1}}{\tau} &= \mathbf{v}_\tau^{k-\frac{1}{2}}, \\ \tau \cdot \mathfrak{R}'_{v_\tau^k} \left(\frac{\mathbf{v}_\tau^k - \mathbf{v}_\tau^{k-1}}{\tau} \right) & \end{aligned}$$

$$\begin{aligned}
 &+ 2 \cdot \mathfrak{E}'_{u_\tau^k} \left(t^k; \mathbf{u}_\tau^{k-\frac{1}{2}}, \mathbf{e}_{2\tau}^{k-\frac{1}{2}}, \alpha_\tau^{k-1} \right) \\
 &+ 2 \cdot \mathfrak{R}'_{v_\tau^k} \left(\mathbf{u}_\tau^{k-1}, \mathbf{e}_{2\tau}^{k-1}, \alpha_\tau^{k-1}; v_\tau^{k-\frac{1}{2}}, \right. \\
 &\quad \left. \frac{\mathbf{e}_{2\tau}^k - \mathbf{e}_{2\tau}^{k-1}}{\tau}, 0 \right) = \mathbf{f}_\tau^k, \\
 &2 \cdot \mathfrak{E}'_{e_{2\tau}^k} \left(t^k; \mathbf{u}_\tau^{k-\frac{1}{2}}, \mathbf{e}_{2\tau}^{k-\frac{1}{2}}, \alpha_\tau^{k-1} \right) \\
 &+ \tau \cdot \mathfrak{R}'_{e_{2\tau}^k} \left(\mathbf{u}_\tau^{k-1}, \mathbf{e}_{2\tau}^{k-1}, \alpha_\tau^{k-1}; v_\tau^{k-\frac{1}{2}}, \frac{\mathbf{e}_{2\tau}^k - \mathbf{e}_{2\tau}^{k-1}}{\tau}, 0 \right) = 0, \\
 &2 \cdot \partial_{\alpha_\tau^k} \mathfrak{E} \left(t^k; \mathbf{u}_\tau^k, \mathbf{e}_{2\tau}^k, \alpha_\tau^{k-\frac{1}{2}} \right) \\
 &+ \tau \cdot \partial_{\alpha_\tau^k} \mathfrak{R} \left(\mathbf{u}_\tau^{k-1}, \mathbf{e}_{2\tau}^{k-1}, \alpha_\tau^{k-1}; 0, 0, \frac{\alpha_\tau^k - \alpha_\tau^{k-1}}{\tau} \right) \ni 0,
 \end{aligned} \tag{14}$$

where $\mathbf{f}_\tau^k = \mathbf{f}(t^k)$.

The discussed variable separation allows Eq. (14) to be seen in a variational manner as stationarity conditions of certain functionals. It requires, however, slight modifications of the system. First, using Eq. (14)₁ and the mid-point value definition, the variable v_τ^k is eliminated from the system by substituting $v_\tau^k = \frac{2}{\tau}(\mathbf{u}_\tau^k - \mathbf{u}_\tau^{k-1}) - v_\tau^{k-1}$ followed by replacing the differentiation with respect to v_τ^k by that with respect to \mathbf{u}_τ^k . Having in mind also convexity of the energy functionals, the relations in Eqs. (14)₂ and (14)₃ represent minimisation conditions for the following convex functional

$$\begin{aligned}
 \mathfrak{H}_{1\tau}^k(\mathbf{u}, \mathbf{e}_2) &= 2 \cdot \mathfrak{R} \left(\frac{\mathbf{u} - \mathbf{u}_\tau^{k-1}}{\tau} - v_\tau^{k-1} \right) \\
 &+ 2 \cdot \mathfrak{E} \left(t^k; \frac{\mathbf{u} + \mathbf{u}_\tau^{k-1}}{2}, \frac{\mathbf{e}_2 + \mathbf{e}_{2\tau}^{k-1}}{2}, \alpha_\tau^{k-1} \right) \\
 &+ \tau \cdot \mathfrak{R} \left(\mathbf{u}_\tau^{k-1}, \mathbf{e}_{2\tau}^{k-1}, \alpha_\tau^{k-1}; \right. \\
 &\quad \left. \frac{\mathbf{u} - \mathbf{u}_\tau^{k-1}}{\tau}, \frac{\mathbf{e}_2 - \mathbf{e}_{2\tau}^{k-1}}{\tau}, 0 \right) - \mathfrak{F}(t^k; \mathbf{u}),
 \end{aligned} \tag{15}$$

which implies that $(\mathbf{u}_\tau^k, \mathbf{e}_{2\tau}^k) = \operatorname{argmin} \mathfrak{H}_{1\tau}^k(\mathbf{u}, \mathbf{e}_2)$. Notice that kinetic energy appears in the functional to be calculated only from the velocity difference.

In a similar way, the last inclusion in Eq. (14) is a condition for finding $\alpha_\tau^k = \operatorname{argmin} \mathfrak{H}_{2\tau}^k(\alpha)$, where

$$\begin{aligned}
 \mathfrak{H}_{2\tau}^k(\alpha) &= 2 \cdot \mathfrak{E} \left(t^k; \mathbf{u}_\tau^k, \mathbf{e}_{2\tau}^k, \frac{\alpha + \alpha_\tau^{k-1}}{2} \right) \\
 &+ \tau \cdot \mathfrak{R} \left(\mathbf{u}_\tau^{k-1}, \mathbf{e}_{2\tau}^{k-1}, \alpha_\tau^{k-1}; 0, 0, \frac{\alpha_\tau^k - \alpha_\tau^{k-1}}{\tau} \right),
 \end{aligned} \tag{16}$$

using the couple $(\mathbf{u}_\tau^k, \mathbf{e}_{2\tau}^k)$ calculated by the minimisation of the functional $\mathfrak{H}_{1\tau}^k$. The proposed staggered

approach, processes these two minimisations within each time step to get the complete solution belonging to the time instant t^k . It should be noticed that the unidirectionality of the degradation process adds a constraint to the minimisation of $\mathfrak{H}_{2\tau}^k$ which is provoked by the conditions $0 \leq \alpha \leq 1$ and $\dot{\alpha} \geq 0$ assumed by Eqs. (3) and (7). In terms of the discretised relations, they can be expressed as $\alpha_\tau^{k-1} \leq \alpha_\tau^k \leq 1$ and implemented directly into constrained quadratic programming algorithms as discussed below.

3.2 Finite element approximation and implementation to quadratic programming algorithms

Looking inside the functionals in Eqs. (2) and (7), it is seen that an appropriate spatial discretisation provides the first minimisation with a quadratic functional $\mathfrak{H}_{1\tau}^k$. Thus, the minimisation may be implemented by a Quadratic Programming (QP) algorithm, as formulated in Dostál (2009) and also applied in previous author works (Vodička et al. 2014; Vodička 2016; Vodička 2023). The functional $\mathfrak{H}_{2\tau}^k$, however, does not have to be quadratic, as the degradation function Φ in Eq. (2) is only assumed to be convex. The minimisation with respect to the phase-field variable thus relies on using QP sequentially—Sequential Quadratic Programming (SQP), see Boggs and Tolle (1995), Björkman et al. (1995) and it is constrained by aforementioned box constraints [below Eq. (16)]. Seeing the solution process within an optimisation algorithm, rather than the commonly used Newton-Raphson methodology for nonlinearities, allows an efficient implementation of various constraints appearing in the solution, though in the present implementation limited to (separately) convex functionals. Details of the computational procedures follow.

The functionals of Eq. (15) contain a split of spherical strain, distinguishing tension and compression, (e.g. $\operatorname{sph}^+ \mathbf{e}$ and $\operatorname{sph}^- \mathbf{e}$) which makes it piecewise quadratic. Computationally, it can be reformulated introducing new variables ψ and ω satisfying additional constraints $\psi \geq 0, \quad \psi + \operatorname{tr} \mathbf{e}(\mathbf{u}) \geq 0,$
 $\omega \geq 0, \quad \omega + \operatorname{tr} \mathbf{e}_2 \geq 0,$ (17) where tr refers to the trace of pertinent tensor. This is a classical scheme, also referred to as a Mosco-type transformation (Mosco 1967).

Discretisation by FEM provides approximation of all variables inside the problem expressed in terms of

their nodal variables and appropriate nodal shape functions. Considering particular mesh with a typical element size h , the formulae for the approximation of the trajectory variables and the newly defined auxiliary variables at the time instant t^k are expressed in the form

$$\begin{aligned} \mathbf{u}_h^k(x) &= \sum_n N_n(x) \mathbf{u}_n^k, \\ \alpha_h^k(x) &= \sum_n N_n(x) \alpha_n^k, \\ \mathbf{e}_{2h}^k(x) &= \sum_n \mathbf{P}_n(x) \mathbf{e}_{2n}^k, \\ \psi_h^k(x) &= \sum_n P_n(x) \psi_n^k, \\ \omega_h^k(x) &= \sum_n P_n(x) \omega_n^k, \end{aligned} \tag{18}$$

introducing nodal variables $\mathbf{u}_n^k, \alpha_n^k, \mathbf{e}_{2n}^k, \psi_n^k, \omega_n^k$ and appropriate nodal shape functions according to the FEM discretisation $N_n(x), P_n(x)$. Matrices generated from them and those necessary for computations include the following ones:

$$\begin{aligned} N_n &= \begin{pmatrix} N_{n,1} & 0 \\ 0 & N_{n,2} \end{pmatrix}, \mathbf{B}_n = \begin{pmatrix} N_{n,1} & 0 \\ 0 & N_{n,2} \end{pmatrix}, \\ \mathbf{P}_n &= \begin{pmatrix} P_n & 0 & 0 \\ 0 & P_n & 0 \\ 0 & 0 & P_n \end{pmatrix}, \bar{N}_n = (N_{n,1} \ N_{n,2}), \end{aligned} \tag{19}$$

where subscripts separated by comma refer to differentiation with respect to the corresponding spatial variable x_1 , or x_2 , cf. Fig. 1. Additionally for the splits in strain variables and the tensor trace, three constant matrices are used

$$\mathbf{S} = \begin{pmatrix} 1 & 1 & 0 \\ 1 & 1 & 0 \\ 0 & 0 & 0 \end{pmatrix}, \mathbf{D} = \begin{pmatrix} 1 & -1 & 0 \\ -1 & 1 & 0 \\ 0 & 0 & 1 \end{pmatrix}, \mathbf{P} = (1 \ 1 \ 0). \tag{20}$$

The approximations are substituted into functionals (2), (5), (7) and evaluated within the discretised functional from Eq. (15). Finally, it is written at the current time step eliminating terms which contain only α^{k-1} , as they do not affect the minimisation with respect to the deformation variables. Such a modified functional $\tilde{\mathfrak{H}}_{1h}^k(\hat{\mathbf{u}}_h, \hat{\mathbf{e}}_{2h}, \hat{\psi}_h, \hat{\omega}_h)$ then reads

$$\begin{aligned} &\tilde{\mathfrak{H}}_{1h}^k(\hat{\mathbf{u}}_h, \hat{\mathbf{e}}_{2h}, \hat{\psi}_h, \hat{\omega}_h) \\ &= \frac{1}{2} \left(1 + \frac{1}{\gamma}\right) \sum_m \sum_n \int_{\Omega} \Phi(\alpha_h^{k-1}) \\ &\quad \left((\mathbf{B}_n (\hat{\mathbf{u}}_n + \mathbf{u}_n^{k-1}) \right. \end{aligned}$$

$$\begin{aligned} &\left. - \mathbf{P}_n (\hat{\mathbf{e}}_{2n} + \mathbf{e}_{2n}^{k-1}) \right)^\top \\ &\times (K_p \mathbf{S} + \mu \mathbf{D}) (\mathbf{B}_n (\hat{\mathbf{u}}_n + \mathbf{u}_n^{k-1}) \\ &- \mathbf{P}_n (\hat{\mathbf{e}}_{2n} + \mathbf{e}_{2n}^{k-1})) \Big) d\Omega + \frac{1}{2} (1 + \gamma) \\ &\times \sum_m \sum_n (\hat{\mathbf{e}}_{2m} + \mathbf{e}_{2m}^{k-1})^\top \left(\int_{\Omega} \Phi(\alpha_h^{k-1}) \right. \\ &\quad \left(\mathbf{P}_m^\top (K_p \mathbf{S} + \mu \mathbf{D}) \mathbf{P}_n \right) d\Omega \Big) (\hat{\mathbf{e}}_{2n} + \mathbf{e}_{2n}^{k-1}) \\ &+ \left(1 + \frac{1}{\gamma}\right) \sum_m \sum_n \hat{\psi}_m \left(\int_{\Omega} (1 - \Phi(\alpha_h^{k-1})) \right. \\ &\quad \left. K_p P_m P_n d\Omega \right) \hat{\psi}_n + (1 + \gamma) \sum_m \sum_n \hat{\omega}_m \\ &\quad \left(\int_{\Omega} (1 - \Phi(\alpha_h^{k-1})) K_p P_m P_n d\Omega \right) \hat{\omega}_n \\ &+ \frac{\tau_{r1}}{\tau} \sum_m \sum_n (\hat{\mathbf{u}}_m - \mathbf{u}_m^{k-1})^\top \left(\int_{\Omega} \hat{\Phi}(\alpha_h^{k-1}) \right. \\ &\quad \left. (\mathbf{B}_m^\top (K_p \mathbf{S} + \mu \mathbf{D}) \mathbf{B}_n) d\Omega \right) (\hat{\mathbf{u}}_n - \mathbf{u}_n^{k-1}) \\ &+ \frac{\tau_{r2}}{\tau} \sum_m \sum_n (\hat{\mathbf{e}}_{2m} - \mathbf{e}_{2m}^{k-1})^\top \left(\int_{\Omega} \hat{\Phi}(\alpha_h^{k-1}) \right. \\ &\quad \left. (\mathbf{P}_m^\top (K_p \mathbf{S} + \mu \mathbf{D}) \mathbf{P}_n) d\Omega \right) (\hat{\mathbf{e}}_{2n} - \mathbf{e}_{2n}^{k-1}) \\ &+ \frac{1}{\tau^2} \sum_m \sum_n (\hat{\mathbf{u}}_m - \mathbf{u}_m^{k-1} - \tau \mathbf{v}_m^{k-1})^\top \\ &\quad \left(\int_{\Omega} \rho N_m^\top N_n d\Omega \right) (\hat{\mathbf{u}}_n - \mathbf{u}_n^{k-1} - \tau \mathbf{v}_n^{k-1}) \\ &- \sum_n \left(\int_{\Gamma_N} \mathbf{f}_{\tau n}^k \cdot N_n d\Gamma \right) \hat{\mathbf{u}}_n, \end{aligned} \tag{21}$$

where values with the superscript index $k - 1$ are available from the previous time step, including \mathbf{v}_n^{k-1} , which is not part of minimisation. The terms which contain only values with index $k - 1$ could have been eliminated from the minimisation as well because they do not have an effect in the minimisation.

Additional constraints on auxiliary variables are provided according to the conditions (17) as follows:

$$\begin{aligned} \hat{\psi}_n &\geq 0, \quad 2\hat{\psi}_n + \bar{N}_n (\hat{\mathbf{u}}_n + \mathbf{u}_n^{k-1}) - \mathbf{P} (\hat{\mathbf{e}}_{2n} + \mathbf{e}_{2n}^{k-1}) \geq 0, \\ \hat{\omega}_n &\geq 0, \quad 2\hat{\omega}_n + \mathbf{P} (\hat{\mathbf{e}}_{2n} + \mathbf{e}_{2n}^{k-1}) \geq 0. \end{aligned} \tag{22}$$

If the nodal values are gathered to column vectors $\hat{\mathbf{u}}_h, \hat{\mathbf{e}}_{2h}, \hat{\psi}_h, \hat{\omega}_h$ as the introduced notation indicates, and the integrals in Eq. (21) are used to determine matrices $\mathbf{K}_{\bullet\bullet}, \mathbf{K}_\bullet, \mathbf{Q}_{\bullet\bullet}$ with indices corresponding to the nodal

values of the function on which they operate, \mathbf{V} which contains \mathbf{v}^{k-1} , and \mathbf{F} which contains \mathbf{f}_τ^k . The matrix form of the functional (21) with constraints (22), which is to be minimised, is given in matrix form as

$$\begin{aligned} & \tilde{\mathfrak{H}}_{1h}^k(\hat{\mathbf{u}}_h, \hat{\mathbf{e}}_{2h}, \hat{\psi}_h, \hat{\omega}_h) \\ &= \begin{pmatrix} \hat{\mathbf{u}}_h \\ \hat{\mathbf{e}}_{2h} \end{pmatrix}^\top \begin{pmatrix} \mathbf{K}_{uu} & \mathbf{K}_{ue_2} \\ \mathbf{K}_{e_2u} & \mathbf{K}_{e_2e_2} \end{pmatrix} \begin{pmatrix} \hat{\mathbf{u}}_h \\ \hat{\mathbf{e}}_{2h} \end{pmatrix} \\ &+ \begin{pmatrix} \mathbf{u}_h^{k-1} \\ \mathbf{e}_{2h}^{k-1} \end{pmatrix}^\top \begin{pmatrix} \mathbf{Q}_{uu} & \mathbf{Q}_{ue_2} \\ \mathbf{Q}_{e_2u} & \mathbf{Q}_{e_2e_2} \end{pmatrix} \begin{pmatrix} \hat{\mathbf{u}}_h \\ \hat{\mathbf{e}}_{2h} \end{pmatrix} \\ &+ \hat{\psi}_h^\top \mathbf{K}_\psi \hat{\psi}_h + \hat{\omega}_h^\top \mathbf{K}_\omega \hat{\omega}_h - (\mathbf{V} + \mathbf{F}) \hat{\mathbf{u}}_h, \end{aligned} \tag{23}$$

where the terms containing only values with index $k - 1$ have been eliminated. Realise that the matrices \mathbf{K} and \mathbf{Q} depend on the values of the phase-field variable and should have been written $\mathbf{K}(\alpha_h^{k-1})$, $\mathbf{Q}(\alpha_h^{k-1})$, as can be read in Eq. (21), however, the notation has been abbreviated.

The minimiser \mathbf{u}_h^k , \mathbf{e}_{2h}^k is obtained by a QP algorithm [implemented by a constrained conjugate gradient based scheme (Dostál 2009)] and provides the nodal displacements and internal strains of the k -th time step, i. e. for $\hat{\mathbf{u}}_h = \mathbf{u}_h^k$, $\hat{\mathbf{e}}_{2h} = \mathbf{e}_{2h}^k$ which determine the (approximated) solution \mathbf{u}_h^k , \mathbf{e}_{2h}^k introduced in Eq. (18). To complete the solution, it is also necessary to calculate velocity needed at least for the next time step calculation. The nodal values are obtained by the formula $\mathbf{v}_n^k = \frac{2}{\tau} (\mathbf{u}_n^k - \mathbf{u}_n^{k-1}) - \mathbf{v}_n^{k-1}$ related to Eq. (14)₁.

Similarly, the substitution of approximations in Eq. (18) into the functional $\mathfrak{H}_{2\tau}^k$ of Eq. (16) and using the definitions in Eqs. (2) and (7) leads to another numerical minimisation.

Before preparing the formula, consider general convexity (which guarantees positivity of its second derivative) of the degradation function Φ in Eq. (2). If it is not merely quadratic, the aforementioned QP algorithm is applied sequentially. It means that the degradation function is approximated by the quadratic Taylor polynomial and the solution is calculated iteratively. Namely, if the iterations within the time step t^k use the index r , in finding the minimum, an iterated functional $\tilde{\mathfrak{H}}_{2,h}^{k,r}(\hat{\alpha}_h)$ is used. It differs from $\mathfrak{H}_{2\tau}^k$ in substituting the approximation and in replacement of the degradation function by its quadratic approximation

$$\begin{aligned} \Phi(\hat{\alpha}_h) &\approx \Phi(\alpha_h^{k,r-1}) + \Phi'(\alpha_h^{k,r-1}) (\hat{\alpha}_h - \alpha_h^{k,r-1}) \\ &+ \frac{1}{2} \Phi''(\alpha_h^{k,r-1}) (\hat{\alpha}_h - \alpha_h^{k,r-1})^2, \end{aligned} \tag{24}$$

where $\alpha_h^{k,r-1}$ is known from the previous sequential iteration.

Now, the functional $\mathfrak{H}_{2\tau}^k$ is written for the current time step after eliminating terms which contain only deformation variables variables or constants (the functional is denoted $\tilde{\mathfrak{H}}_{2,h}^{k,r}$), which have no effect in minimisation with respect to the phase-field variable α . It reads

$$\begin{aligned} & \tilde{\mathfrak{H}}_{2,h}^{k,r}(\hat{\alpha}_h) = \\ & \sum_n \left(\int_{\Omega^n} (\Phi'(\alpha_h^{k,r-1}) - \alpha_h^{k,r-1} \Phi''(\alpha_h^{k,r-1})) \right. \\ & \left((K_p |\text{sph}^+ \mathbf{e}_{2h}^k|^2 + \mu |\text{dev} \mathbf{e}_{2h}^k|^2) (1 + \gamma) \right. \\ & \left. + (K_p |\text{sph}^+(\mathbf{e}(\mathbf{u}_h^k) - \mathbf{e}_{2h}^k)|^2 \right. \\ & \left. + \mu |\text{dev}(\mathbf{e}(\mathbf{u}_h^k) - \mathbf{e}_{2h}^k)|^2) (1 + \frac{1}{\gamma}) \right) N_n \, d\Omega \Big) \hat{\alpha}_n \\ & + \sum_m \sum_n \hat{\alpha}_m \left(\int_{\Omega^n} \frac{1}{2} \Phi''(\alpha_h^{k,r-1}) \left((K_p |\text{sph}^+ \mathbf{e}_{2h}^k|^2 \right. \right. \\ & \left. \left. + \mu |\text{dev} \mathbf{e}_{2h}^k|^2) (1 + \gamma) \right) \right. \\ & \left. + (K_p |\text{sph}^+(\mathbf{e}(\mathbf{u}_h^k) - \mathbf{e}_{2h}^k)|^2 \right. \\ & \left. + \mu |\text{dev}(\mathbf{e}(\mathbf{u}_h^k) - \mathbf{e}_{2h}^k)|^2) (1 + \frac{1}{\gamma}) \right) N_m N_n \, d\Omega \Big) \hat{\alpha}_n \\ & + \sum_n \left(\int_{\Omega^n} \frac{3}{8\epsilon} G_c (\mathbf{u}_h^{k-1}, \mathbf{e}_{2h}^{k-1}) N_n \, d\Omega \right) \hat{\alpha}_n \\ & + \sum_m \sum_n \hat{\alpha}_m \left(\int_{\Omega^n} \frac{3\epsilon}{8} G_c^1 \bar{\mathbf{N}}_m \bar{\mathbf{N}}_n^\top \, d\Omega \right) \hat{\alpha}_n. \end{aligned} \tag{25}$$

If the nodal values are written into a column vector $\hat{\alpha}_h$ according to the previous notation, and the integrals in Eq. (25) are used to introduce matrices \mathbf{K}_α , \mathbf{Q}_α . The numerical minimisation then looks for the optimal values of $\hat{\alpha}_h$ for the constrained functional

$$\begin{aligned} & \tilde{\mathfrak{H}}_{2,h}^{k,r}(\hat{\alpha}_h) = \hat{\alpha}_h^\top \mathbf{K}_\alpha (\alpha_h^{k,r-1}, \mathbf{u}_h^k) \hat{\alpha}_h \\ & + \mathbf{Q}_\alpha (\alpha_h^{k,r-1}, \mathbf{u}_h^k, \mathbf{u}_h^{k-1}, \mathbf{e}_{2h}^{k-1}) \hat{\alpha}_h, \quad \alpha_h^{k-1} \leq \hat{\alpha}_h \leq 1, \end{aligned} \tag{26}$$

with constraints obtained from those introduced below Eq. (16). Both matrices in Eq. (26) depend on the values of variables calculated previously. These dependences are stressed in the relation.

The minimum within each iteration is obtained by a constrained conjugate gradient scheme of a QP algorithm, the minimiser is denoted $\alpha_h^{k,r}$ and determines the nodal values (for $\hat{\alpha}_h = \alpha_h^{k,r}$) of the approximation $\alpha_h^{k,r}$ introduced in Eq. (18).

Table 1 A pseudo-code for the phase-field dynamic fracture computational approach

Algorithm : PF_FRAC_DYN($T, \tau, h, \mathbf{u}_0, \mathbf{v}_0, \mathbf{e}_{20}, \alpha_0, f, g$)

```

comment: Solution in the range  $[0, T]$ , the initial conditions are  $\mathbf{u}_0, \mathbf{v}_0, \mathbf{e}_{20}, \alpha_0$ 
 $(\mathbf{u}_h^0, \mathbf{e}_{2h}^0, \psi_h^0, \omega_h^0) \leftarrow (\mathbf{u}_0, \mathbf{v}_0, \mathbf{e}_{20}, \alpha_0)$ 
 $k \leftarrow 0, \quad t \leftarrow 0$ 
while  $t < T$ 
     $k \leftarrow k + 1, \quad t \leftarrow t + \tau$ 
    comment: QP –  $\tilde{\mathfrak{H}}_1^k$ , Eqs. (22) and (23), boundary conditions defined by  $f, g$ 
     $(\mathbf{u}_h^k, \mathbf{e}_{2h}^k, \psi_h^k, \omega_h^k) \leftarrow \operatorname{argmin} \tilde{\mathfrak{H}}_1^k(\hat{\mathbf{u}}_h, \hat{\mathbf{e}}_{2h}, \hat{\psi}_h, \hat{\omega}_h)$ 
     $\mathbf{v}_h^k \leftarrow \frac{2}{\tau} (\mathbf{u}_h^k - \mathbf{u}_h^{k-1}) - \mathbf{v}_h^{k-1}$ 
    comment: SQP –  $\tilde{\mathfrak{H}}_2^k$ , in an iteration approximated by  $\tilde{\mathfrak{H}}_{2,h}^{k,r}$ , Eq. (26)
    do
         $\alpha_h^{k,0} \leftarrow \alpha_h^{k-1}$ 
         $\alpha_h^{k,1} \leftarrow \operatorname{argmin} \tilde{\mathfrak{H}}_{2,h}^{k,1}(\hat{\alpha}_h)$ 
         $r \leftarrow 1$ 
        while  $\|\alpha_h^{k,r} - \alpha_h^{k,r-1}\| > \delta_0$  comment: Predefined convergence criterion
            do
                 $r \leftarrow r + 1$ 
                 $\alpha_h^{k,r} \leftarrow \operatorname{argmin} \tilde{\mathfrak{H}}_{2,h}^{k,r}(\hat{\alpha}_h)$ 
             $\alpha_h^k \leftarrow \alpha_h^{k,r}$ 
         $(\mathbf{u}_h, \mathbf{v}_h, \mathbf{e}_{2h}, \alpha_h) \leftarrow (\mathbf{u}_h^k, \mathbf{v}_h^k, \mathbf{e}_{2h}^k, \alpha_h^k)$  comment: Collecting all results
    return  $(\mathbf{u}_h, \mathbf{v}_h, \mathbf{e}_{2h}, \alpha_h)$ 

```

3.3 Notes on the computer implementation

The whole calculation applied recursively up to given time T is schematically specified in a pseudo-code PF_FRAC_DYN in Table 1. As input arguments it uses boundary conditions included in Eqs. (3) and (4), and initial conditions introduced in Eq. (9). Also notice that the time-stepping value τ (an input value in the PF_FRAC_DYN code) is kept constant throughout the calculation in accordance with the time discretisation in Eq. (14) and the assumptions in the paragraph above it, though it could have been set to different values depending on the damage growth. Moreover, to get accurately wave propagation within a fast rupture process, the Courant–Friedrich–Lewy (CFL) condition (Courant et al. 1928) was taken into account, which states $\tau < h/v_P$ where v_P denotes the wave speed (the speed of sound) in the material. The relation between the time step and the element size was respected in calculations by putting τ slightly smaller than determined by the FEM mesh-size h . For computations, the approach was implemented in an in-house MATLAB computer code which is below used for crack propagation testing under time dependent loads.

4 Examples

We demonstrate the developed numerical approach in a series of calculations. First, the instant of crack nucleation is related to the velocity of propagation of the waves inside the materials, as any information, including effect of the external load, needs some time to be delivered to a particular place. In the second part, typical problems evaluated also by other authors are used to check the influence of the parameters which affect the crack propagation. Namely, parameters of the rheological model and fracture energy.

4.1 Elastic wave propagation causing crack nucleation

First, it is checked how propagating elastic wave provokes a crack nucleation when sufficient energy is at the disposal. A simple domain configuration shown in Fig. 2 together with given boundary conditions make the problem to be essentially one dimensional with the only varying coordinate being x_2 . The given displacement load shown also in Fig. 2 provides a single peak strain energy wave to move in vertical direction from each horizontal face. When these waves meet at the centre, there is sufficient energy to provoke damage, unless the waves are damped due to viscoelastic properties.

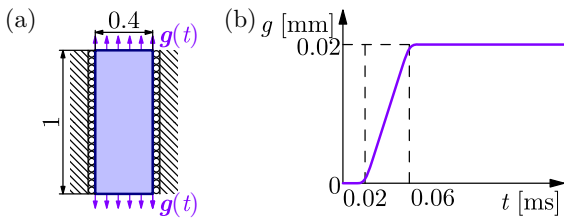


Fig. 2 Simple configuration (a) exposed to a smoothed displacement jump (b)

The initial elastic properties [as introduced in Eq. (2)] are: $K_p = 2\text{ MPa}$, $\mu = 1\text{ MPa}$, the mass density is $\rho = 750\text{ t m}^{-3}$. These values indicate the elastic wave to propagate at the velocity of 2 m s^{-1} (P-wave). What is varied here, is the amount of viscosity expressed by the values of the material parameters τ_{r1} and τ_{r2} . The smoothed displacement jump loading $g(t)$ is described by the function

$$\zeta_1(t; n, w, a, b) = \frac{(2n + 1)!}{(n!)^2 4^{n+1} w} \int_{-w}^w \left(1 - \left(\frac{x}{w}\right)^2\right)^n \cdot \left(1 + \frac{|t - x - a|}{b - a} + \frac{|t - x - b|}{a - b}\right) dx \quad (27)$$

as $g(t) = 0.02\text{ mm} \cdot \zeta_1(t; 4, 10\ \mu\text{s}, 20\ \mu\text{s}, 60\ \mu\text{s})$ and shown in Fig. 2 and it is applied with a time step of $2\ \mu\text{s}$.

The fracture energy in the material is $G_c^I = 7\text{ J m}^{-2}$ and the phase-field length parameter is chosen $\epsilon = 10\ \mu\text{m}$. The PFM degradation function Φ is taken in the basic quadratic form: $\Phi(\alpha) = (1 - \alpha)^2 + 10^{-6}$. The mesh is regular, made of 16,000 square bilinear elements.

The results study the propagation of the wave inside material at the velocity given by the material parameters (and checked by data in the graphics) and initiation of degradation of the material as documented in Fig. 3. The strain energy density ω of the simulation wave is shown in the bottom half of the domain due to a symmetry.

As it is seen, close to the time instant $t = 0.28\text{ ms}$, the waves initiated at the opposite ends of the domain made contact with each other at the centre ($x_2 = 0.5\text{ mm}$) The varying values of the time relaxation parameters τ_{r1} , τ_{r2} affect the appearance of the wave and degradation process, in relation to the fact that increasing values include more attenuation, more energy is dissipated and eventually, if damping is sufficiently high, there is not sufficient energy to initiate damage. Here, this occurred for the largest value of $10\ \mu\text{s}$. The ampli-

tude of the wave decreases due to damping caused by the rheological model and after a wave crush also by a release of energy caused by new crack formation. The release of energy is proportional to the value of the fracture energy.

The values of the phase-field parameter α close to the vertical centre of the domain can be read in Fig. 4. They do not include those $10\ \mu\text{s}$ cases where α is unmodified from the initial value 0. The α distribution pertains to a crack appeared at the instant when the waves met (close to the aforementioned instant of $t = 0.28\text{ ms}$). It is also observed that due to dissipation particular instants of triggering damage vary.

The second example demonstrates the dependence of crack nucleation for a propagating wave on the parameter of fracture energy. The design of the computational experiment was motivated by a similar test made in Weinberg and Wieners (2022). The domain is generated by a curved bar given parametrically as $(x_1, x_2) = (p_1 + p_2 \sin(\frac{\pi}{2} p_1), (1 + p_2) \cos(\frac{\pi}{2} p_1))$, for $|p_1| \leq 0.5\text{ mm}$, $|p_2| \leq 0.03125\text{ mm}$. It is loaded by two slightly unsymmetrical force pulses applied at both ends of the rod, see Fig. 5. The force load is applied as a pulse whose time dependence is expressed by the function

$$\zeta_2(t; c, w, v) = \exp\left(-\Theta(w - v|t - c|) \frac{(v(t - c))^2}{w^2 - (v(t - c))^2}\right) \quad (28)$$

with Θ being the Heaviside step function. Then the forces f_1 and f_2 in Fig. 5 are given by the relations: $f_1(t) = 1\text{ MPa} \cdot \zeta_2(t; 75\ \mu\text{s}, 0.15\text{ mm}, 2\text{ m s}^{-1})$, $f_2(t) = 1.05\text{ MPa} \cdot \zeta_2(t; 90\ \mu\text{s}, 0.15\text{ mm}, 2\text{ m s}^{-1})$.

The elastic properties of the undamaged material are: $K_p = 3\text{ MPa}$, $\mu = 1\text{ MPa}$, the mass density is $\rho = 1000\text{ t m}^{-3}$, so that the elastic P-wave propagates at the velocity of 2 m s^{-1} . Here, the values of the time relaxation related to the schematic dampers in Fig. 1 of viscoelasticity are $\tau_{r1} = \tau_{r2} = 1\ \mu\text{s}$.

The fracture energy of the material considers two values of G_c^I : 3 J m^{-2} and 4 J m^{-2} simultaneously with the value of G_c^{II} , see Eq. (6), such that $G_c^{II} = 5G_c^I$ to reduce the influence of shear. The phase-field length parameter is chosen $\epsilon = 10\ \mu\text{m}$. The PFM degradation function Φ is the same as above. The mesh is regular, made of square bilinear elements of the size $h = 1\ \mu\text{m}$, the load is applied in time steps of the magnitude $1\ \mu\text{s}$.

The changed fracture energy caused different crack-ing. Check the graphics in Fig. 6 to see that with the smaller value of G_c^I the crack appears earlier. The evo-

Fig. 3 Strain energy density ω distribution along the bottom half of the domain at selected instants (values of t in the legend in [ms]) of the simple configuration under a stress-pulse for various viscosity parameters: **a** varying τ_{r1} , vanishing τ_{r2} ; **b** varying τ_{r2} , vanishing τ_{r1} . Values of pertinent τ_{ri} according to the line style: solid $0 \mu\text{s}$, dashed $0.1 \mu\text{s}$, dashdotted $1 \mu\text{s}$, dotted $10 \mu\text{s}$

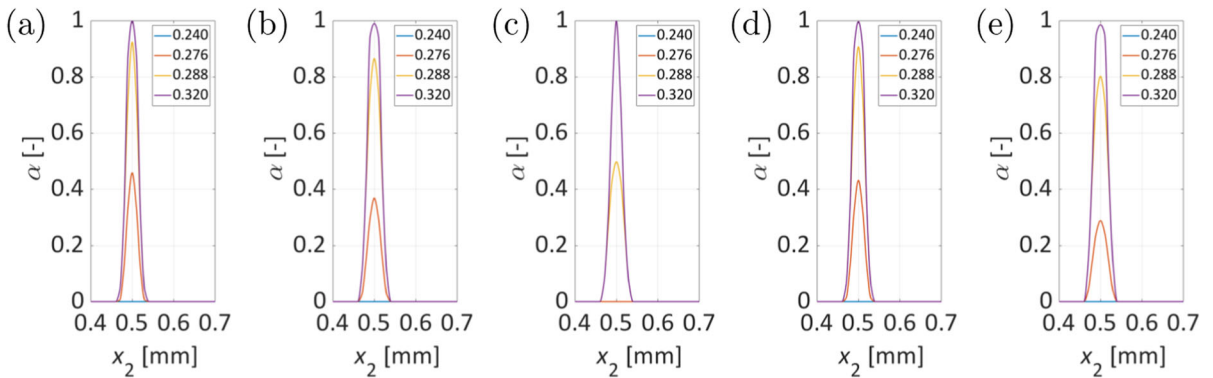
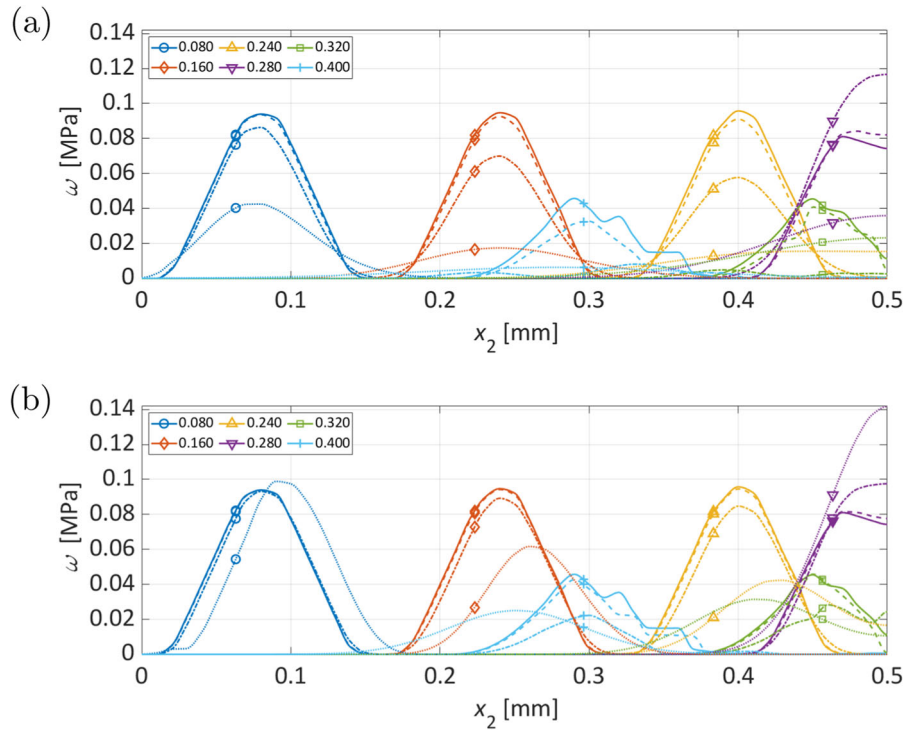
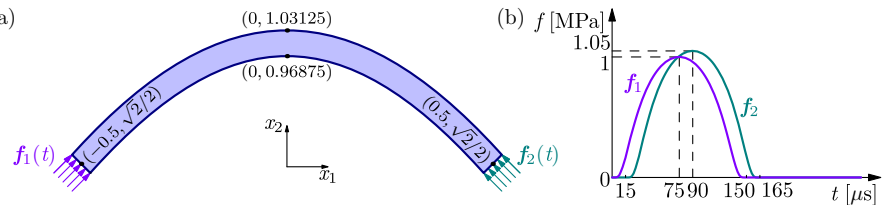


Fig. 4 Phase-field parameter distribution at the central part of the domain at selected instants (legend values in [ms]) of the simple configuration for various viscosity parameters: **a** both zero, **b** $\tau_{r1} = 0.1 \mu\text{s}$, **c** $\tau_{r1} = 1 \mu\text{s}$, **d** $\tau_{r2} = 0.1 \mu\text{s}$, **e** $\tau_{r2} = 1 \mu\text{s}$

Fig. 5 Curved bar (a) exposed to force pulses (b)



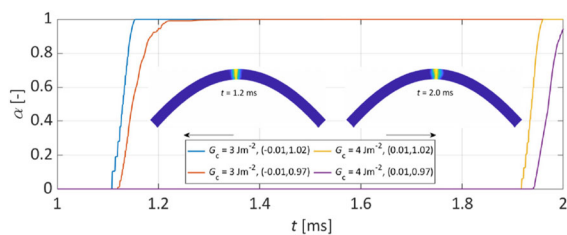


Fig. 6 Evolution of phase-field parameter α in the curved rod case at the particular points (x_1, x_2) of the top and the bottom boundary of the domain where the crack appears, two different values of G_c are used. The enclosed graphics show the actual position of the crack and the time instants when the crack reached the bottom contour

lution of the phase-field variable at two particular points of the domain top and bottom layers is in accordance with the position of the resulting crack shown in the interior drawing pertinent to the time instant $t = 1.2$ ms.

Due to non-symmetry of the load it is not symmetrically located.

When the fracture energy is changed to the other value, this first wave does not have sufficient intensity to provoke a damage leading to a crack, only when the wave is reflected and returned to this central location a crack appears at the instant $t = 2.0$ ms. Also the exact position of the crack is slightly different from the previous one.

The propagation of the elastic wave is documented by a plot of a stress quantity in Figs. 7 and 8.

The first selected instants show the same results up to the moment when at the case of the smaller G_c^I a crack is formed. It is seen that the first compressive waves reach the centre approximately for $t = 0.45$ ms, corresponding to the wave propagation velocity. When it returns in form of tension the intensity is sufficient to produce a crack at the instant $t = 1.2$ ms, if the fracture energy is $G_c^I = 3 \text{ Jm}^{-2}$.

The other case needed the wave to be reflected once more at the bar ends, and only afterwards the crack appears corresponding to the instant $t = 2$ ms as also shown before. Based on the governing relations (9) and functionals (2) and (7), the critical stress value appears to be proportional to the square root of fracture energy (provided that the phase-field parameter ϵ is kept unchanged). The ratio of the fracture energies of the two options provides $\sqrt{4/3} \approx 1.15$ which may be verified by observing the maximal stress values: For $G_c^I = 3 \text{ Jm}^{-2}$ the maximum is seen at Fig. 7g as approx.

1.3 MPa (the same as in Fig. 8g pertaining to the other G_c^I), and for $G_c^I = 4 \text{ Jm}^{-2}$ it is seen at Fig. 8l as approx. 1.5 MPa. Anyhow, the distribution of the stress nicely documents how the waves move and reflect inside the domain.

4.2 Tensile load

Dynamic crack propagation is studied in a problem of a rectangular domain with a pre-crack loaded by a force load. The pre-crack supposed to span across a half of the domain width, shown as Γ_c in Fig. 9. The applied time dependent load is also shown in the same graphics, the function which controls it is. To simplify the calculation because of the symmetry, only the upper part of the domain is considered as documented in the same figure.

The particular geometry was captured from Borden et al. (2012), Li et al. (2023) where similar analysis was done, leading to, as it is going to be presented below, the crack bifurcation or kinking if only the symmetric geometric part is considered. The bifurcation is shown in the calculations made in Vodička (2024).

The initial elastic properties are: $K_p = 22.22 \text{ GPa}$, $\mu = 13.33 \text{ GPa}$, the mass density is $\rho = 2450 \text{ kg m}^{-3}$. These parameters cause the P-wave to propagate at the velocity of 3.81 km s^{-1} , while the Rayleigh wave speed is 2.13 km s^{-1} . The parameters defining the rheology according to the scheme in Fig. 1 are $\gamma = 1$, $\tau_{r2} = 0$, and τ_{r1} being changed in the range from $0.01 \mu\text{s}$ to $10 \mu\text{s}$. The mesh is regular made of 8000 bilinear square elements.

The fracture energy in the domain is $G_c^I = 3 \text{ J m}^{-2}$, and it is slightly modified for the shear mode: $G_c^{II} = 2G_c^I$. The phase-field length parameter is set to $\epsilon = 1 \text{ mm}$. The PFM degradation function Φ is chosen simply the same as in the previous example. The loading $f(t) = 1 \text{ MPa} \cdot \zeta_1(t; 4, 1 \mu\text{s}, 4 \mu\text{s}, 12 \mu\text{s})$ according to Eq. (27) and the graph in Fig. 9 is applied with a refined time step of $0.1 \mu\text{s}$, after an initiation (smoothed linear) period it is kept constant.

The crack propagation processes are studied in terms of the phase-field variable. Its distribution determines the actual position of the crack at each instant, and its changing in time provides the velocity of the crack propagation. As the crack tip is not exactly defined a fixed value 0.9 of the phase-field nodal values is chosen to identify the physical crack and its change within a time span. The graphs in Fig. 10 contain calculated val-

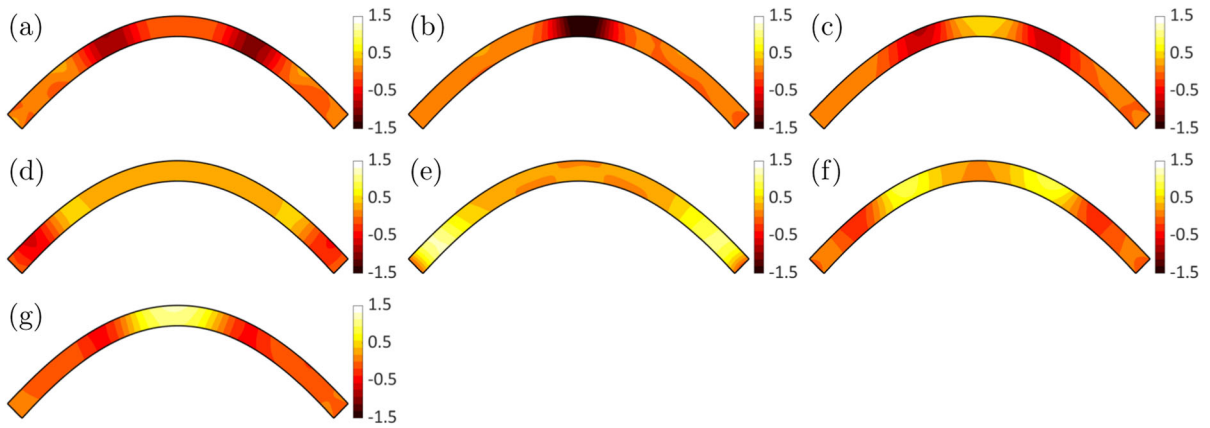


Fig. 7 Distribution of the stress trace [MPa] in the curved rod case, corresponding time instants are: **a** $t = 0.3$ ms, **b** $t = 0.45$ ms, **c** $t = 0.55$ ms, **d** $t = 0.75$ ms, **e** $t = 0.85$ ms, **f** $t = 1$ ms, **g** $t = 1.1$ ms, the fracture energy is $G_c^I = 3 \text{ Jm}^{-2}$

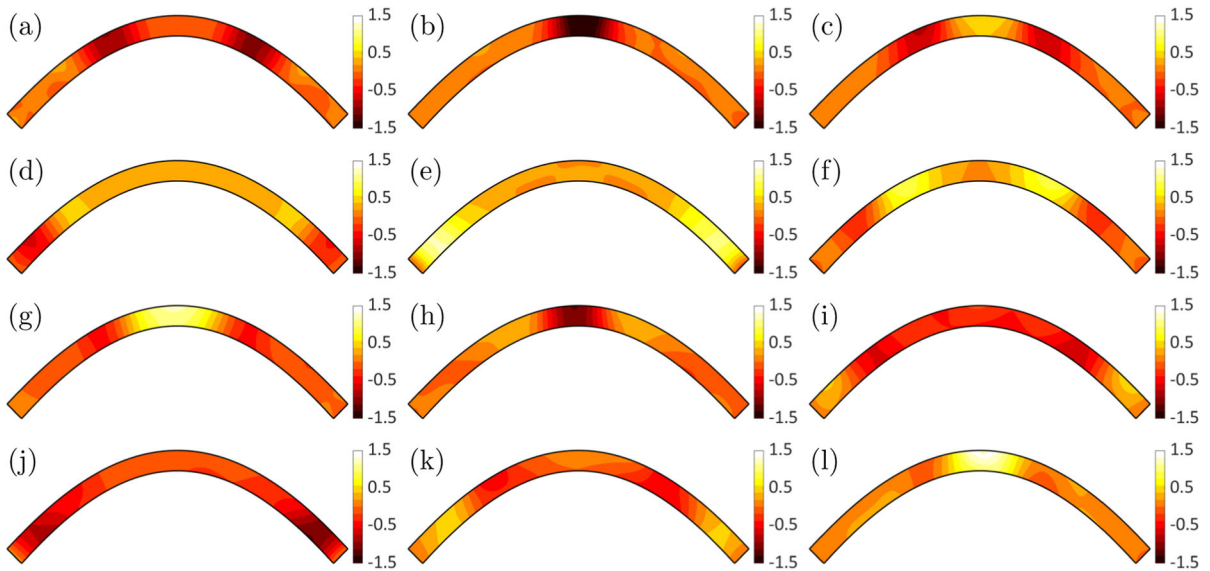


Fig. 8 Distribution of the stress trace [MPa] in the curved rod case, corresponding time instants, additional to those used in Fig. 7 are: **h** $t = 1.24$ ms, **i** $t = 1.44$ ms, **j** $t = 1.55$ ms, **k** $t = 1.66$ ms, **l** $t = 1.92$ ms, the fracture energy is $G_c^I = 4 \text{ Jm}^{-2}$

ues of this velocity expressed in terms of the Rayleigh wave speed. It is seen how the parameter τ_r affects the crack propagation: the instant of triggering the evolution of α and also the speed at which the crack elongates.

First, the instants when the cracks start to propagate are observed: approximately $t = 30 \mu\text{s}$ for the smallest values of τ_{r1} gradually increasing to more than $t = 40 \mu\text{s}$ for the largest selected τ_{r1} . The increasing time relaxation parameter has also effect on the crack propagation. The crack propagates slower, and

also the position of the point where crack changes from its straight direction to two bifurcated crack moves to the left. For this symmetric case only one of these two cracks is obtained and looks like kinking of the original crack direction.

Four instants were chosen to demonstrate the actual distribution of the phase-field variable α and pertinent stress state expressed in terms of stress trace $\text{tr} \sigma$ and the norm of the deviatoric stress $\text{dev} \sigma$. When plotting α , the deformations are magnified in order to visualise the opening character of the crack which is identified

Fig. 9 Configuration for the tensile load (a) where only a half of the domain is considered in the calculation (b) exposed to a prescribed force (c)

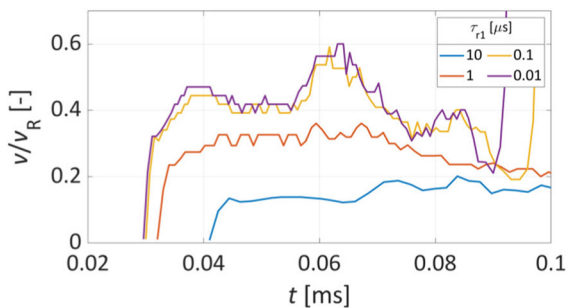
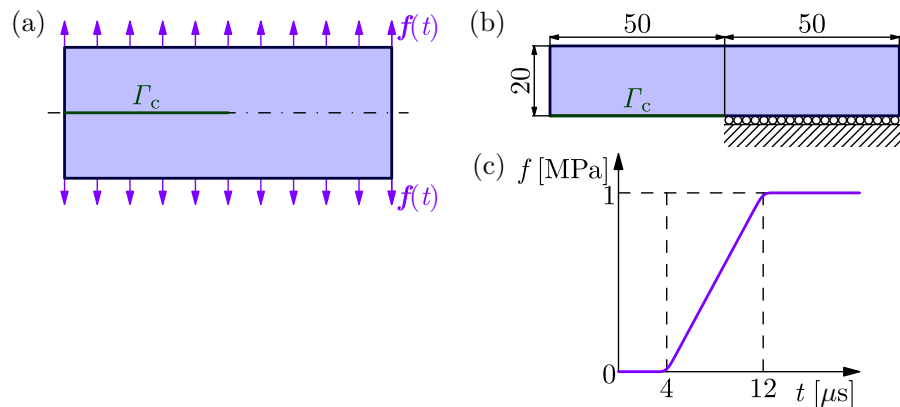


Fig. 10 Crack propagation velocity in the tensile load case depending on relaxation time parameter τ_{r1} (the other keeping zero) in terms of the Rayleigh wave speed v_R

insight the light a white zone pertinent to $\alpha = 1$. The instants are pertinent, at least approximately, to crack initiation, straight crack propagation, kinking of the crack and the end point of the time range $t = 100 \mu\text{s}$.

Graphics in Figs. 11, 12, 13 pertain to the most viscous case. The α plot shows that the crack starts to kink very early after it starts to propagate. The crack tip stress concentration tracks the damage towards the upper face, where later appears compression, caused by bending. Nevertheless an excess of deviatoric stress causes the damage to be also initiated at this upper face.

Situation is totally different for the case with small viscosity shown in Figs. 14, 15, 16. Here, the crack propagates more rapidly and there is a long straight part of the crack. Only afterwards the crack kinks and finally the crack propagation terminates by total separation of the upper loaded part. The shear stress in the upper layer is not so large to attract the crack propagation, which is additionally faster as in the previous case, see also Fig. 10. Anyhow, the stress concentration close to the crack tip can be identified with the values correspond-

ing to the formula derived in Vodička (2023) for the case without viscosity. It is used as a simplified approximation if τ_{ri} are sufficiently small, and its formula for the critical stress values: $\frac{(\text{tr}^+\sigma)_c^2}{2K_p G_c^I} + \frac{|\text{dev}\sigma|_c^2}{\mu G_c^{II}} = \frac{-3}{2\epsilon\Phi'(0)}$ is adjusted according to the present data. The relation $\frac{(\text{tr}^+\sigma)_c^2}{133.33\text{MPa}^2\text{mm}} + \frac{|\text{dev}\sigma|_c^2}{80\text{MPa}^2\text{mm}} = 0.75\text{mm}^{-1}$ is obtained which is approximately satisfied by the values detected at the instant of damage initiation: $\text{tr}\sigma \approx 9 \text{ MPa}$, $|\text{dev}\sigma| \approx 3 \text{ MPa}$.

As it was seen, the bifurcated cracks make changes in the stress distribution possibly leading to zones with high shear stress where a crack may be initiated. Therefore, consideration of the mode mixity in defining the fracture energy introduced in Eq. (6) is important, though no detailed description of the phenomenon is provided here. Additionally, the rheological properties may modify the crack formation processes in materials.

The results are surely affected by the discretisation. The mesh size was required to be sufficiently small relative to the length-scale parameter ϵ , with the time step satisfies the CFL condition as mentioned in Sect. 3.3. Anyhow, it can be checked how the solution behaves for somehow coarser discretisations. The solution for the case with $\tau_{r1} = 0.1 \mu\text{s}$ (Figs. 14, 15, 16) was recalculated in two such discretisations and the results in terms of the phase-field variable α are shown in Figs. 17, and 18.

Both initiation of the crack propagation and the crack speed document how mesh refinement improves the numerical data in refinements made in agreement with proportionality of time and space discretisation made in Sect. 3.3.

Fig. 11 Distribution of the phase-field variable α in the tensile load case shown with a magnified deformation ($\times 50$), corresponding time instants are: **a** $t = 30 \mu\text{s}$, **b** $t = 55 \mu\text{s}$, **c** $t = 75 \mu\text{s}$, **d** $t = 100 \mu\text{s}$, the time relaxation parameter $\tau_{r1} = 10 \mu\text{s}$

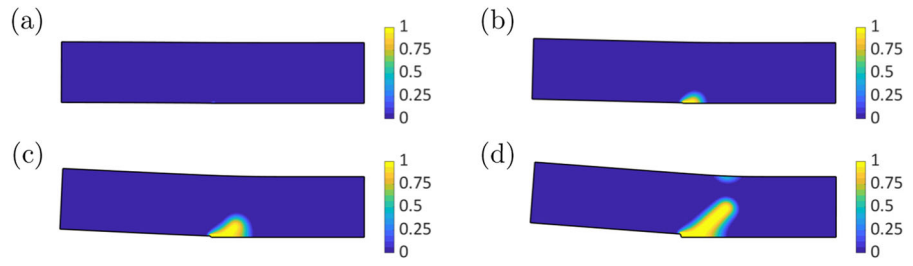


Fig. 12 Distribution of the stress trace [MPa] in the tensile load case, corresponding time instants are: **a** $t = 30 \mu\text{s}$, **b** $t = 55 \mu\text{s}$, **c** $t = 75 \mu\text{s}$, **d** $t = 100 \mu\text{s}$, the time relaxation parameter $\tau_{r1} = 10 \mu\text{s}$

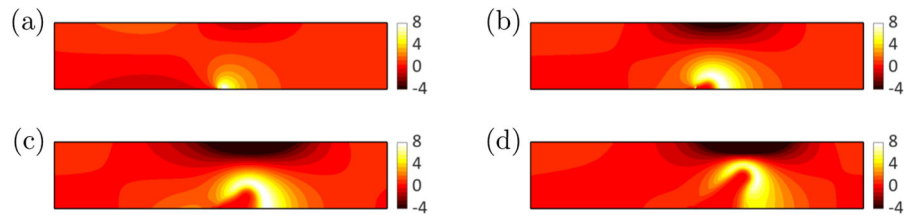
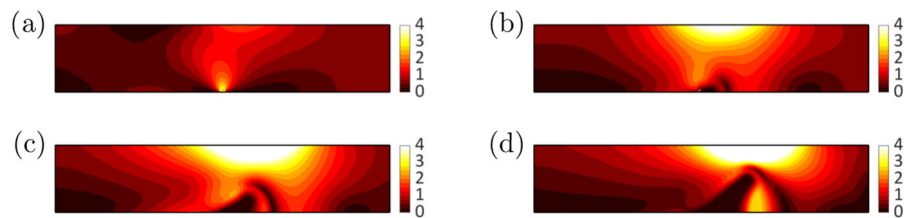


Fig. 13 Distribution of the norm of deviatoric stress [MPa] in the tensile load case, corresponding time instants are: **a** $t = 30 \mu\text{s}$, **b** $t = 55 \mu\text{s}$, **c** $t = 75 \mu\text{s}$, **d** $t = 100 \mu\text{s}$, the time relaxation parameter $\tau_{r1} = 10 \mu\text{s}$



4.3 Lateral compression with a shear character

Another situation occurs if the load is applied so that the pre-crack is loaded as in the shear mode. Such a case occurs for a known Kalthoff–Winkler experiment, which is to be considered in this section. The pre-crack is again supposed to span across a half of the domain width, shown as Γ_c in Fig. 20. The applied increasing displacement load is also shown in the same graphics, the function which controls it is $g(t; s) = 16.5 \text{ ms}^{-1} \cdot \frac{1}{4s} ((t + s)^2 - |t - s| \cdot (t - s) - 2s^2)$ for $s = 1 \mu\text{s}$. Also here, the calculation is simplified by considering symmetry as shown in part (b) of the figure.

It has to be mentioned that the element size in the coarsest mesh is larger than the parameter ϵ , still the solution seems to be reasonable, only the crack propagation is much smaller. This velocity can also be checked in Fig. 19.

Similar conditions were also considered in Borden et al. (2012), Li et al. (2023) and in accordance with experimental observation a inclined crack was obtained

computationally. The same situation is considered here, with a small study of dependence on the fracture energy.

The initial elastic properties are: $K_p = 182.69 \text{ GPa}$, $\mu = 73.08 \text{ GPa}$, the mass density is $\rho = 8000 \text{ kg m}^{-3}$. These parameters cause the P-wave to propagate at the velocity of 5.65 km s^{-1} , while the Rayleigh wave speed is 2.80 km s^{-1} . The parameters defining the rheology are $\gamma = 1$, $\tau_{r2} = 1 \mu\text{s}$, and $\tau_{r1} = 1 \mu\text{s}$. The mesh is regular, made of 62,500 bilinear square elements.

The minimal fracture energy in the domain is $G_c^c = 2.766 \text{ kJ m}^{-2}$, so that in calculation there are used the values $G_c^I = r G_c^c$, for $r = 1, 2, 4, 8$ and respectively increased value for the shear mode: $G_c^{II} = q G_c^I$, for $q = 1, 10$. The phase-field length parameter is set to $\epsilon = 0.5 \text{ mm}$ and the same degradation function as before.

The graphs in Fig. 21 contain calculated values of this velocity expressed in terms of the Rayleigh wave speed. They show how the fracture energy (expressed by ratio parameters r and q) affects the crack propagation: the instant of triggering the evolution of phase-

Fig. 14 Distribution of the phase-field variable α in the tensile load case shown with a magnified deformation ($\times 50$), corresponding time instants are: **a** $t = 30 \mu\text{s}$, **b** $t = 55 \mu\text{s}$, **c** $t = 75 \mu\text{s}$, **d** $t = 100 \mu\text{s}$, the time relaxation parameter $\tau_{r1} = 0.1 \mu\text{s}$

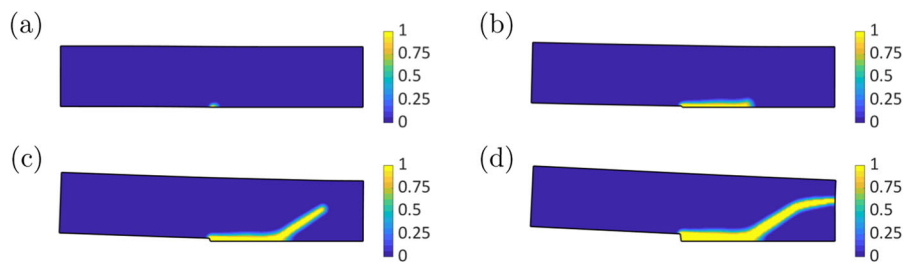


Fig. 15 Distribution of the stress trace [MPa] in the tensile load case, corresponding time instants are: **a** $t = 30 \mu\text{s}$, **b** $t = 55 \mu\text{s}$, **c** $t = 75 \mu\text{s}$, **d** $t = 100 \mu\text{s}$, the time relaxation parameter $\tau_{r1} = 0.1 \mu\text{s}$

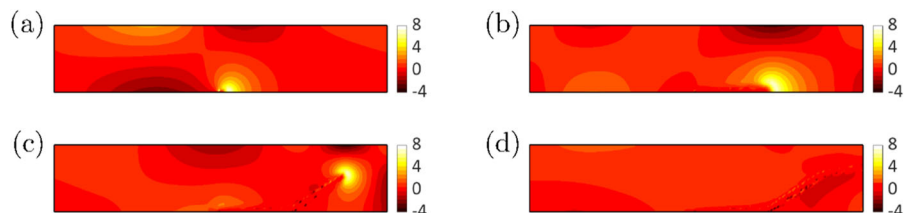


Fig. 16 Distribution of the norm of deviatoric stress [MPa] in the tensile load case, corresponding time instants are: **a** $t = 30 \mu\text{s}$, **b** $t = 55 \mu\text{s}$, **c** $t = 75 \mu\text{s}$, **d** $t = 100 \mu\text{s}$, the time relaxation parameter $\tau_{r1} = 0.1 \mu\text{s}$

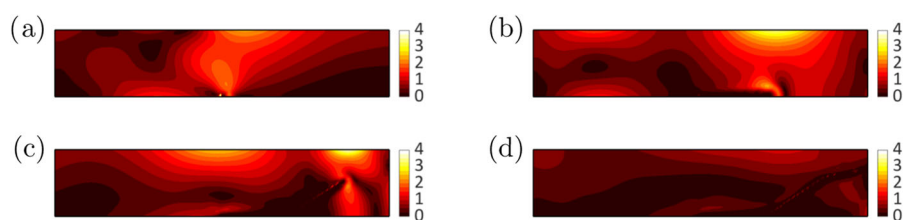


Fig. 17 Distribution of the phase-field variable α in the tensile load case shown with a magnified deformation ($\times 50$); corresponding time instants are the same as in Fig. 14, while the FEM mesh size and the time step are four times larger ($h = 2 \text{ mm}$ $\tau = 0.4 \mu\text{s}$)

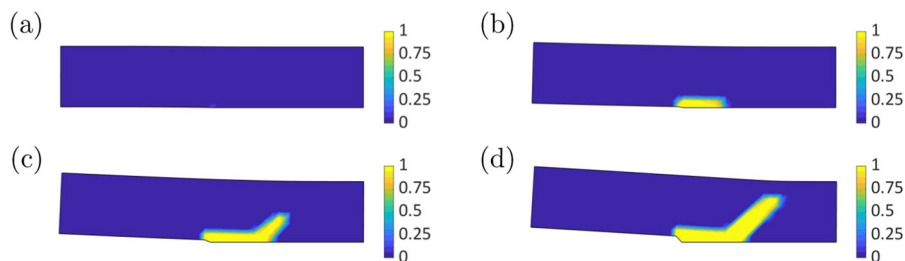
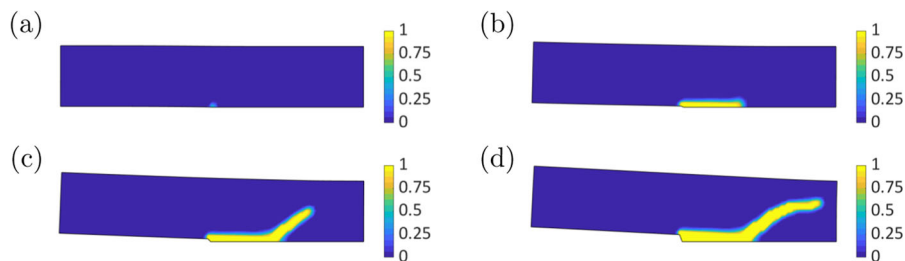


Fig. 18 Distribution of the phase-field variable α in the tensile load case shown with a magnified deformation ($\times 50$); corresponding time instants are the same as in Fig. 14, while the FEM mesh size and the time step are two times larger ($h = 1 \text{ mm}$ $\tau = 0.2 \mu\text{s}$)



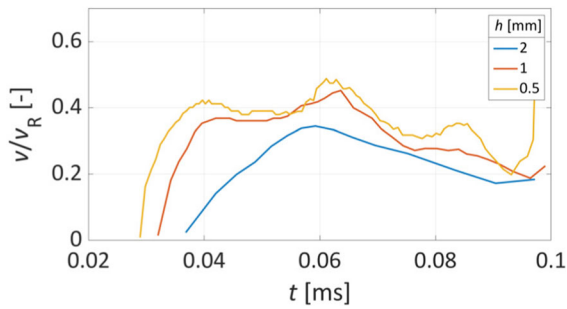


Fig. 19 Crack propagation velocity in the tensile load case depending on discretisation (FEM mesh size h), $\tau_{r1} = 0.1 \mu\text{s}$. The values of the time steps are (in the same order): $0.4 \mu\text{s}$, $0.2 \mu\text{s}$, $0.1 \mu\text{s}$

field variable and also the speed at which the crack elongates.

It is also observed that decreasing value of fracture energy increases the crack propagation velocity. Increasing only the G_c^{II} part of the fracture energy also affects the crack propagation as it suppresses the influence of the deviatoric part of the stress or strain variables. With the smallest value of the fracture energy, there is a different evolution of the analysed crack speed, which is caused by the change of a crack pattern appearing inside the domain in the calculation: additionally to the inclined crack which appears at the pre-crack tip in all cases, there appears also another

Fig. 20 Configuration for the lateral compression load (a) where only a half of the domain is considered in the calculation (b) exposed to a given time-dependent force load (c)

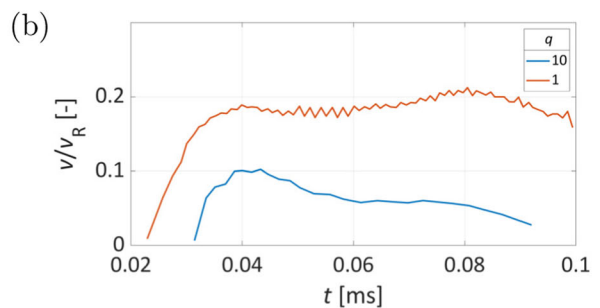
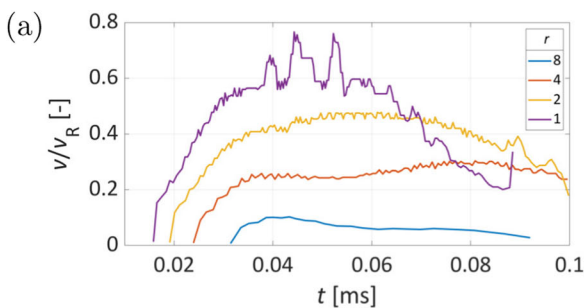
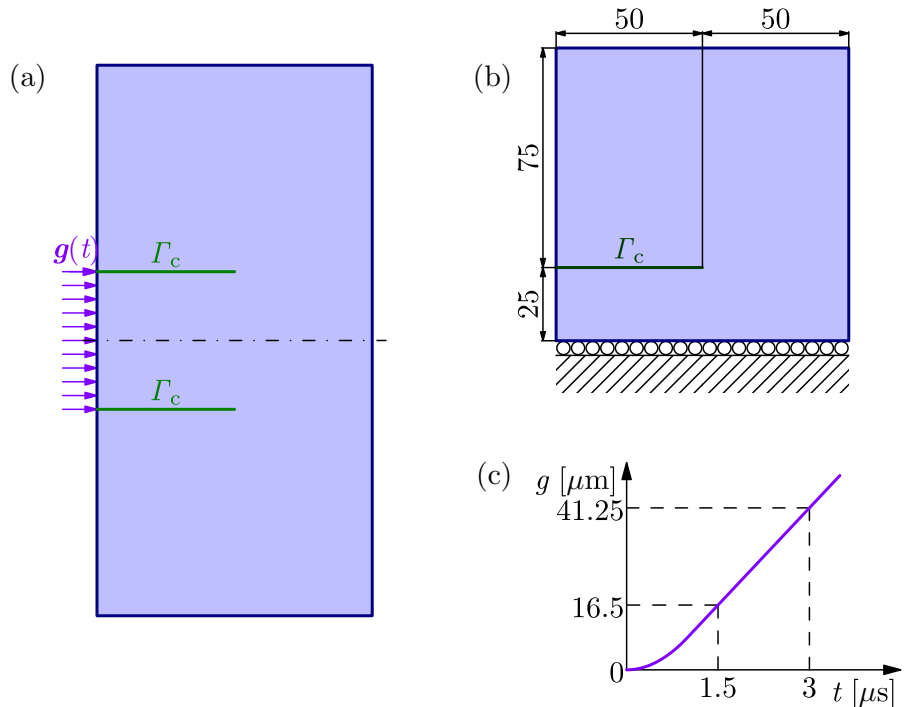


Fig. 21 Crack propagation velocity in the lateral compression case depending on fracture energy: **a** $G_c^{\text{I}} = rG_c^{\text{c}}$, keeping $G_c^{\text{II}} = 10G_c^{\text{I}}$, and **b** $G_c^{\text{II}} = qG_c^{\text{I}}$, keeping $G_c^{\text{I}} = 8G_c^{\text{c}}$ in terms of the Rayleigh wave speed v_R

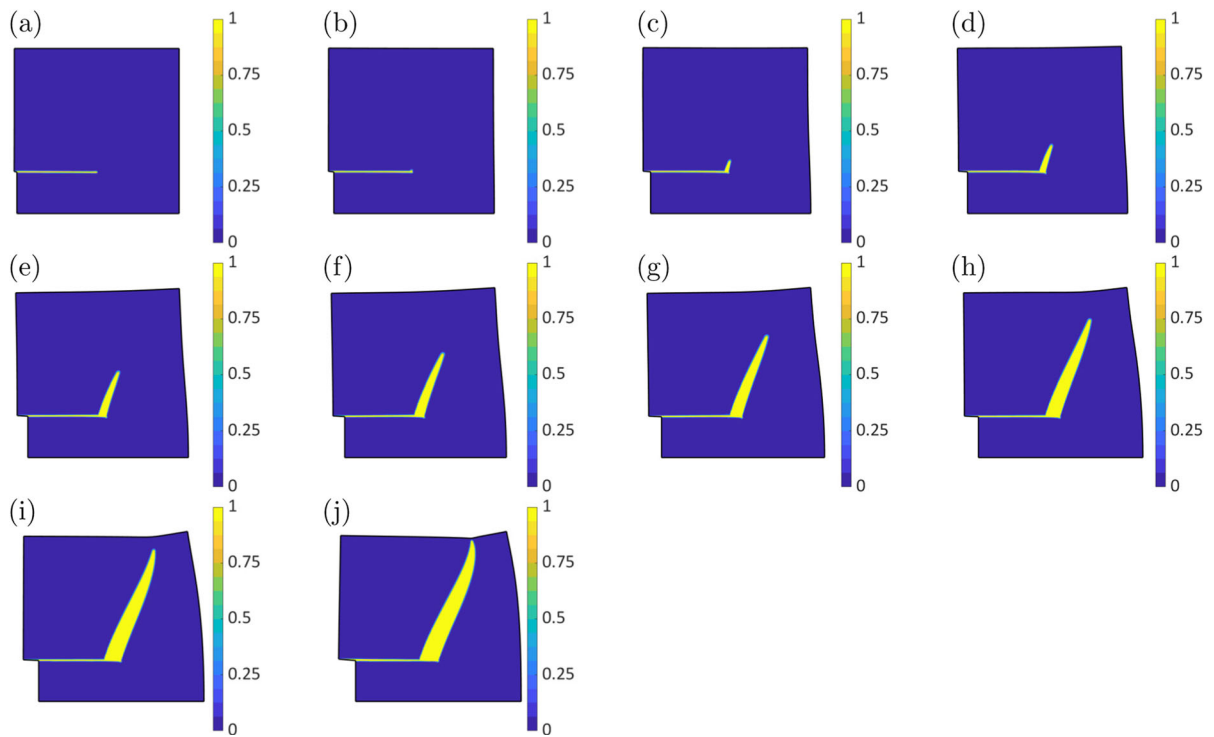


Fig. 22 Distribution of the phase-field variable α in the lateral compression case, corresponding time the instants: **a** to **j** starting for $t = 10\mu\text{s}$ and the step $100\tau = 10\mu\text{s}$ the fracture energy is $G_c^I = 2G_c^c$, $G_c^{II} = 10G_c^I$

crack caused by the tensile forces at the right side, see the cracking description in Fig. 34 below.

Crack propagation and pertinent stress distribution document what affects the processes leading to rupture in this structural element. The first choice of the parameter pertain to the case of $r = 2$ and $q = 10$. It documents in detail in Figs. 22, 23, 24 how the propagating wave of strain energy inside material causes the initiation and propagation of the crack which is inclined with respect to the direction of the pre-crack at an angle of about $\frac{2\pi}{5}$ corresponding to the observations of Borden et al. (2012), Li et al. (2023). In the first of the figures the series of instants show how the crack propagates. Comparing to the other two where stresses are shown, it is seen how the originally compressive wave is reflected as tensional and provokes the crack propagation initialised by a stress concentration near the crack tip. Both volumetric and deviatoric stresses contribute to the overall stress state and thus feed strain energy, though the contribution of the deviatoric part is reduced by modifying the shear fracture energy. With an intent to estimate the strength of the material (with fixed

parameter ϵ), the general formula of Sect. 4.2 for determining the critical stress values is used. The current data provide $\frac{(\text{tr}^+\sigma)_c^2}{2.021\text{GPa}^2\text{mm}} + \frac{|\text{dev}\sigma|_c^2}{4.042\text{GPa}^2\text{mm}} = 1.5\text{mm}^{-1}$ and for damage initiation corresponding to the parts (b) of Figs. 22, 23, 24 it is verified by the following values: $\text{tr}\sigma \approx 1.6\text{ GPa}$, $|\text{dev}\sigma| \approx 0.8\text{ GPa}$. These values appear approximately near the crack tip for all snapshots.

The reasonability of the applied discretisation is documented by comparing the results to coarser ones. As in the previous example, two discretisations with the doubled mesh size and time step size are used. The velocity of crack propagation is depicted in Fig. 25 for three such options.

The results of the finest case, used also in Figs. 22, 23, 24, seem to be adequate for the sequence of refined meshes and time steps.

The observation is also complemented by plotting the crack profiles for the coarser meshes in Figs. 26 and 27.

Here, the coarsest mesh result in the former graphic is larger than the parameter ϵ , as in the analysis in

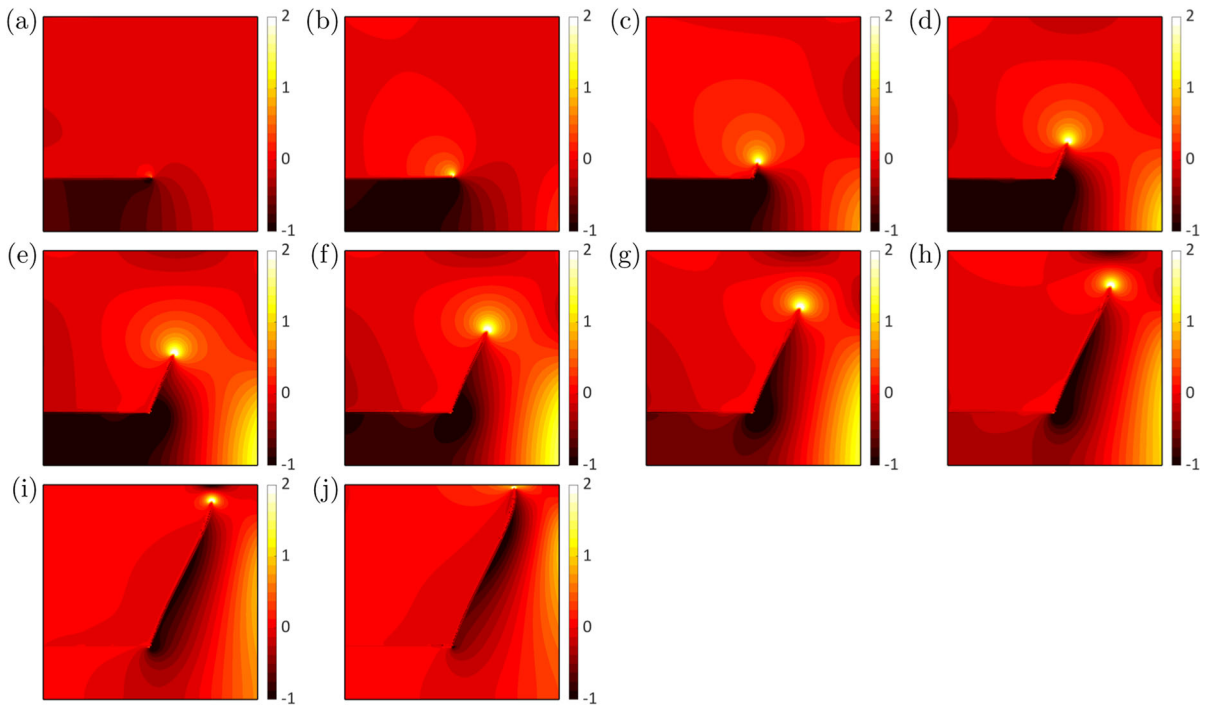


Fig. 23 Distribution of the stress trace [GPa] in the lateral compression case, corresponding time the same instants and fracture energies as in Fig. 22

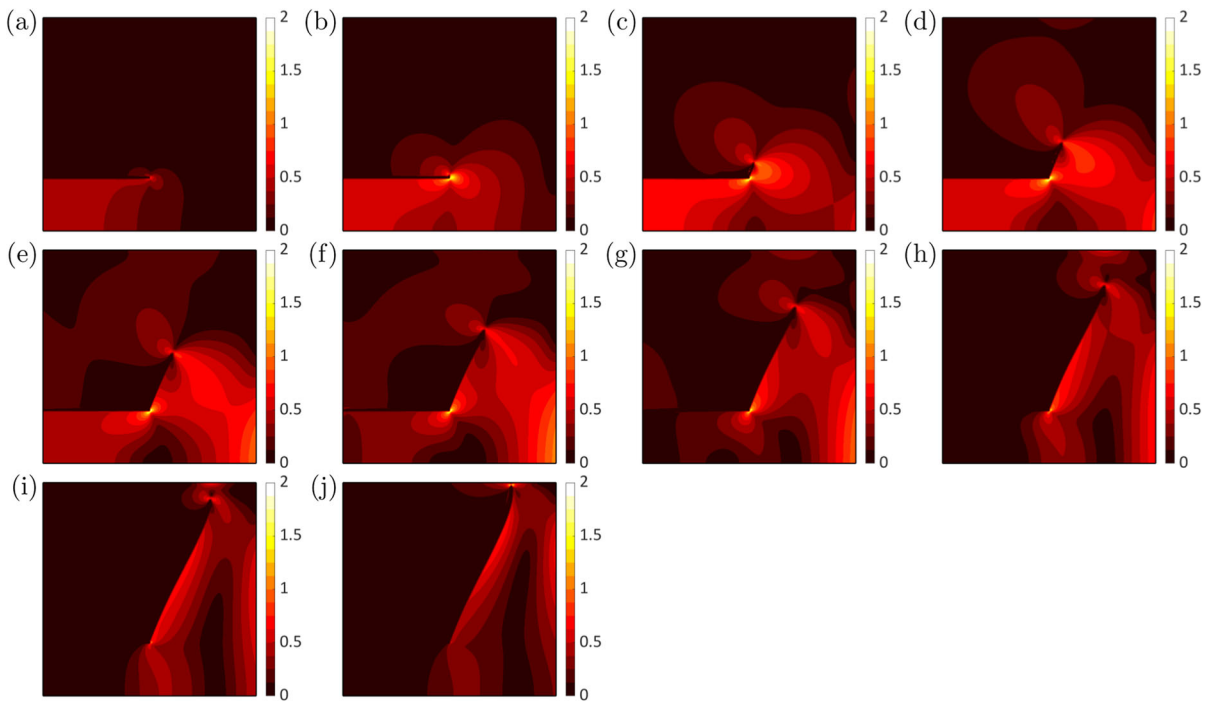


Fig. 24 Distribution of the norm of the deviatoric stress [GPa] in the lateral compression case, corresponding time the same instants and fracture energies as in Fig. 22

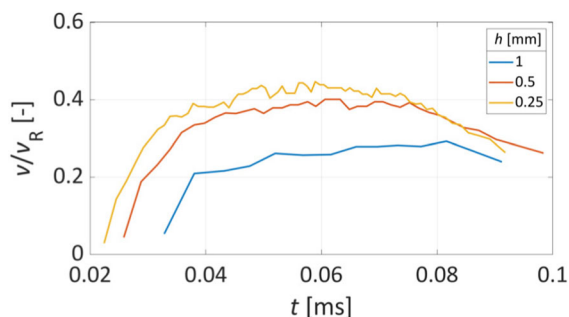


Fig. 25 Crack propagation velocity in the lateral compression case depending on discretisation (FEM mesh size h), pertinent to the fracture energy $G_c^I = 2G_c^C$, $G_c^{II} = 10G_c^I$. The values of the time steps are (in the same order): $0.4 \mu\text{s}$, $0.2 \mu\text{s}$, $0.1 \mu\text{s}$

Sect. 4.2, though the solution is rather satisfactory comparing to the finer cases.

The description of cracking is modified if the parameters of fracture conditions are modified, too. If, first, the fracture energy is increased, then there is not sufficient energy for a massive crack propagation and, comparing also to Fig. 21, there appears only a short crack within the given time range. There are only four snapshots selected in Figs. 28, 29, 30 to see that the wave has passed over the stress concentration at the crack tip without significant increase of the crack length.

The modified G_c provide $\frac{(\text{tr}^+\sigma)_c^2}{8.085\text{GPa}^2\text{mm}} + \frac{|\text{dev}\sigma|_c^2}{16.17\text{GPa}^2\text{mm}} = 1.5\text{mm}^{-1}$, and for situation corresponding to the parts (d) of Figs. 28, 29, 30 it is verified by the values: $\text{tr}\sigma \approx 3.3 \text{ GPa}$, $|\text{dev}\sigma| \approx 1.2 \text{ GPa}$. At the last snapshot, the pictures (j), the stresses are substantially lower so that the crack stopped propagating.

Now, the deviatoric stress part is allowed to contribute to cracking by decreasing the shear fracture energy. It naturally provides faster crack propagation documented by the same selected instants (as in the

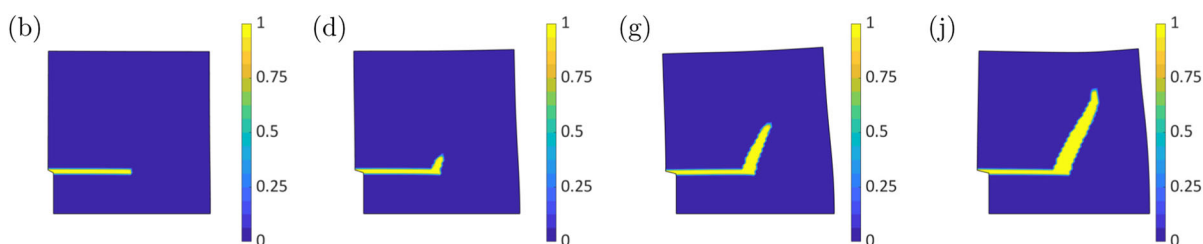


Fig. 26 Distribution of the phase-field variable α in the lateral compression case case shown with a magnified deformation ($\times 50$), the time instants (b), (d), (g), (j) refer to those introduced

previous calculation) in Figs. 31, 32, 33. Additionally, there appears also another crack at the original crack tip, which, however, is in the compression zone and thus it is caused by shear. There appears a question in which physical situation such cracking mechanism may occur.

Finally, as it was already mentioned, the calculated crack pattern may be different as obtained in the calculation with a low fracture energy, where another crack appeared caused by the tensile forces at the lower right corner (symmetric case). Such a crack was not observed in experimental results, though some numerical data reference also this Li et al. (2023), one of the reasons might be lowness of the fracture toughness in calculation. Also this crack, however, is bifurcated as caused by the tensile force in the previous calculation in Sect. 4.2. The corresponding graphs for this case are shown in Fig. 34.

5 Conclusions

A quasi-brittle fracture computational model is introduced for load applied generally causing a mixed-mode cracking. The solution process is controlled by time dependent displacement or force load which requires to consider also inertial forces. At the same time, material is considered with some rheological properties which includes a kind of damping in strain wave propagation and alters the process related to crack propagation. The material viscosity is introduced by an accepted four parametric model, within which any of the simple solid-like rheological models like Kelvin-Voigt or Poynting-Thomson can be seen as special choices when the material parameters are accordingly adjusted.

in Fig. 22 (compare), the FEM mesh size and the time step are four times larger ($h = 1 \text{ mm}$ $\tau = 0.4 \mu\text{s}$)

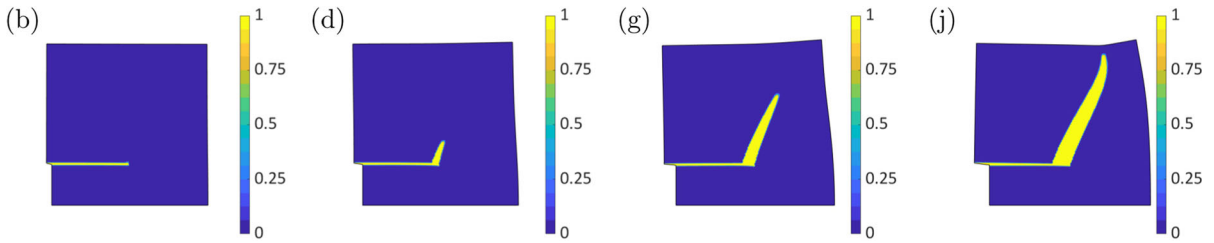


Fig. 27 Distribution of the phase-field variable α the lateral compression case case shown with a magnified deformation ($\times 50$), the time instants (b), (d), (g), (j) refer to those introduced in

Fig. 22 (compare), the FEM mesh size and the time step are two times larger ($h = 0.5 \text{ mm}$ $\tau = 0.2 \mu\text{s}$)

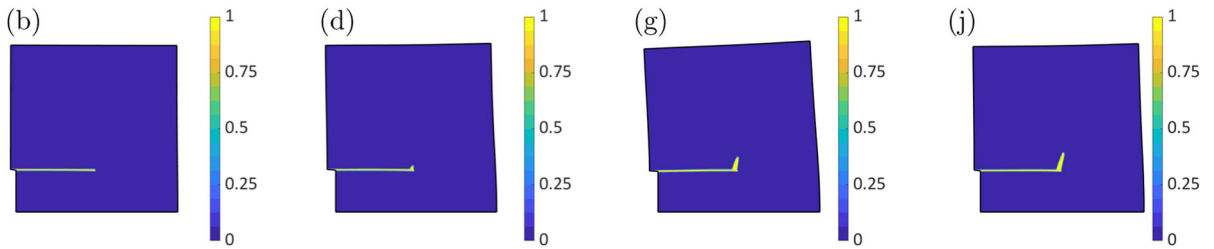


Fig. 28 Distribution of the phase-field variable α in the lateral compression case, corresponding time the instants (b), (d), (g), (j) in Fig. 22, the fracture energy is $G_c^I = 8G_c^c$, $G_c^{II} = 10G_c^I$

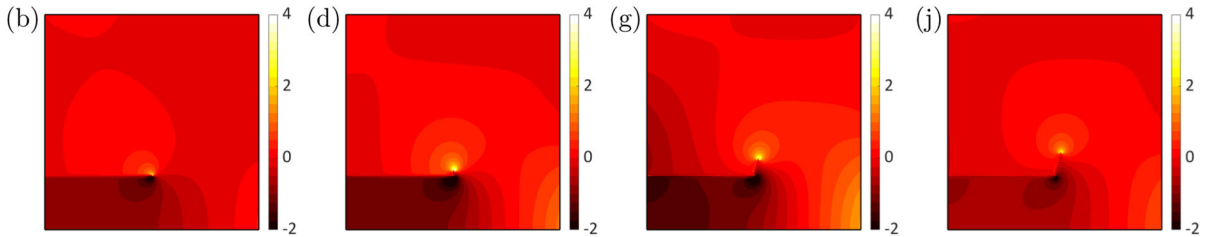


Fig. 29 Distribution of the stress trace [GPa] in the lateral compression case, corresponding time the same selected instants and fracture energies as in Fig. 28

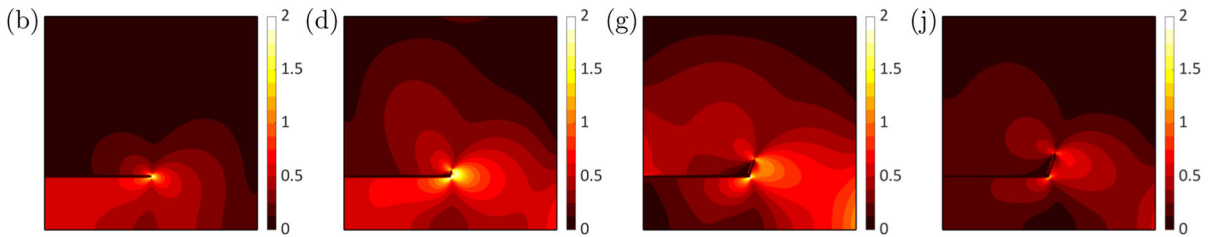


Fig. 30 Distribution of the norm of the deviatoric stress [GPa] in the lateral compression case, corresponding time the same instants and fracture energies as in Fig. 28

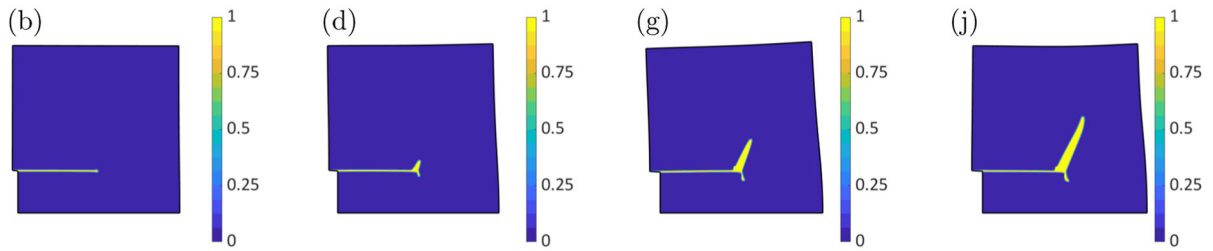


Fig. 31 Distribution of the phase-field variable α in the lateral compression case, corresponding time the instants (b), (d), (g), (j) in Fig. 22, the fracture energy is $G_c^I = 8G_c^c$, $G_c^{II} = G_c^I$

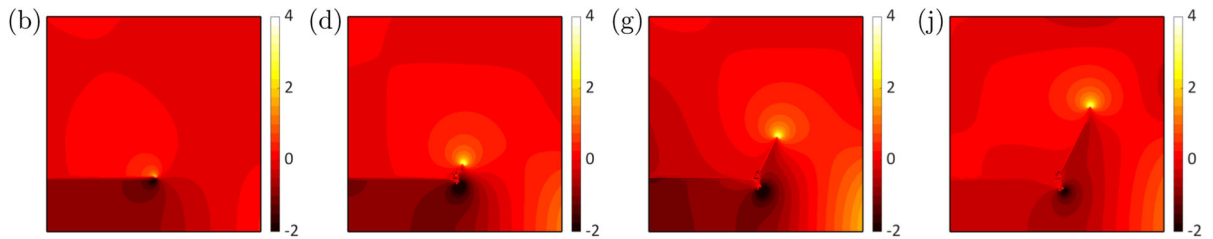


Fig. 32 Distribution of the stress trace [GPa] in the lateral compression case, corresponding time the same instants and fracture energies as in Fig. 31

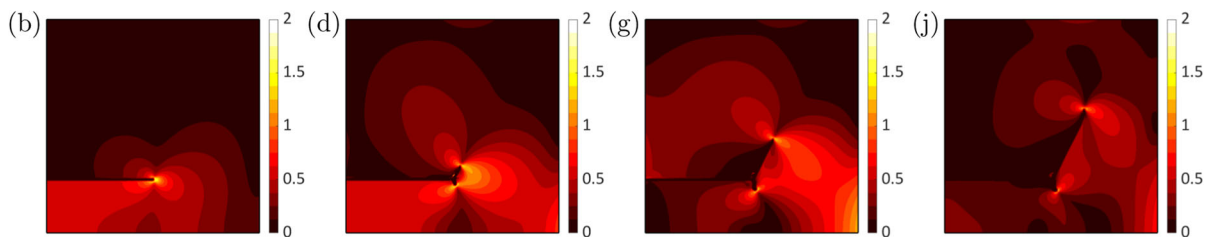


Fig. 33 Distribution of the norm of the deviatoric stress [GPa] in the lateral compression case, corresponding time the same instants and fracture energies as in Fig. 31

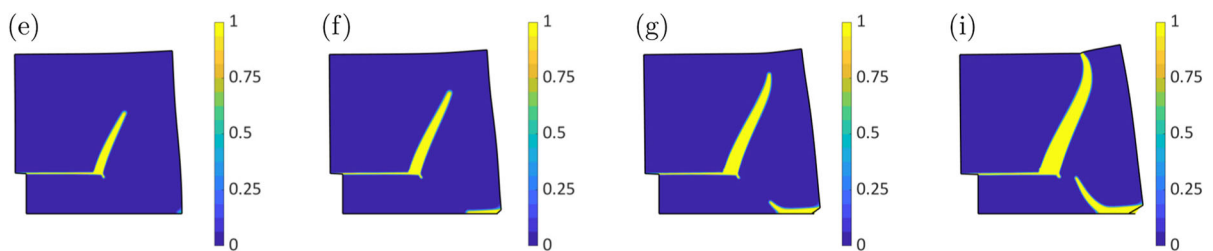


Fig. 34 Distribution of the phase-field variable α in the lateral compression case, corresponding time the instants (e), (f), (g), (i) in Fig. 22, the fracture energy is $G_c^I = G_c^c$, $G_c^{II} = 10G_c^I$

The model, of course, requires also parameters pertinent to crack formation processes, those which are stressed by the present approach allow to distinguish mixity of the fracture mode. Naturally, the values of such parameters modify degradation processes in mate-

rials as it was presented within the numerical calculations, their accurate adjustment and calibration have to be done in comparison with experimental measurements.

There were also described some details of the implementation of the computational approach. Remarkably its basic features, it includes a staggered time stepping which provided the computational scheme to have a variational character. And it directly provoked implementation of sequential quadratic programming to the algorithm, equipped with the spatial discretisation by a finite element approach. All such computational details were put into practice in the in-house MATLAB code.

Following the presented results it is believed that the computational approach will be adequate also in other calculations for dynamic crack propagation. Additionally, it is intended to extend the present computational model to the case which includes also interfacial damage and fracture in a forthcoming paper.

Acknowledgements The author acknowledges support by the grants VEGA 1/0363/21 and VEGA 1/0307/23.

Author contributions R.V. conceived, designed and performed analysis; designed, implemented and verified computational code; wrote the manuscript text and prepared all the graphics.

Funding Open access funding provided by The Ministry of Education, Science, Research and Sport of the Slovak Republic in cooperation with Centre for Scientific and Technical Information of the Slovak Republic

Data availability No datasets were generated or analysed during the current study.

Declarations

Conflict of interest The authors declare no competing interests.

Open Access This article is licensed under a Creative Commons Attribution 4.0 International License, which permits use, sharing, adaptation, distribution and reproduction in any medium or format, as long as you give appropriate credit to the original author(s) and the source, provide a link to the Creative Commons licence, and indicate if changes were made. The images or other third party material in this article are included in the article's Creative Commons licence, unless indicated otherwise in a credit line to the material. If material is not included in the article's Creative Commons licence and your intended use is not permitted by statutory regulation or exceeds the permitted use, you will need to obtain permission directly from the copyright holder. To view a copy of this licence, visit <http://creativecommons.org/licenses/by/4.0/>.

References

Ambrosio L, Tortorelli VM (1990) Approximation of functional depending on jumps by elliptic functional via Γ -convergence. *Commun Pure Appl Math* 43(8):999–1036

- Bedford A (1985) Hamilton's principle in continuum mechanics. Pitman, Boston
- Bourdin B, Francfort GA, Marigo JJ (2000) Numerical experiments in revisited brittle fracture. *J Mech Phys Solids* 48:797–826
- Bourdin B, Francfort GA, Marigo JJ (2008) The variational approach to fracture. *J Elast* 91:5–148
- Björkman G, Klarbring A (1995) Sequential quadratic programming for non-linear elastic contact problems. *Int J Numer Methods Eng* 38:137–165
- Benzeggagh ML, Kenane M (1996) Measurement of mixed-mode delamination fracture toughness of unidirectional glass/epoxy composites with mixed-mode bending apparatus. *Compos Sci Technol* 56:439–449
- Boggs PT, Tolle JW (1995) Sequential quadratic programming. *Acta Numer* 4:1–51
- Borden MJ, Verhoosel CV, Scott MA, Hughes TJR, Landis CM (2012) A phase-field description of dynamic brittle fracture. *Comput Methods Appl Mech Eng* 217–220:77–95
- Courant R, Friedrichs K, Lewy H (1928) Über die partiellen differenzgleichungen der mathematischen physik. *Math Ann* 100:32–47
- Crank J, Nicolson P (1947) A practical method for numerical evaluation of solutions of partial differential equations of the heat conduction type. *Proc Camb Philos Soc* 43:50–67
- Cao Y, Wang W, Shen W, Cui X, Shao J (2022) A new hybrid phase-field model for modeling mixed-mode cracking process in anisotropic plastic rock-like materials. *Int J Plast* 157:103395
- Dal Maso G (2012) An introduction to Γ -convergence. *Progress in nonlinear differential equations and their applications*, vol 8. Springer, New York
- Dostál Z (2009) Optimal quadratic programming algorithms. *Springer optimization and its applications*, vol 23. Springer, Berlin
- Del Piero G (2013) A variational approach to fracture and other inelastic phenomena. *J Elast* 112:3–77
- Feng Y, Li J (2022) Phase-field cohesive fracture theory: a unified framework for dissipative systems based on variational inequality of virtual works. *J Mech Phys Solids* 159:104737
- Francfort GA, Marigo J-J (1998) Revisiting brittle fracture as an energy minimization problem. *J Mech Phys Solids* 46(8):1319–1342
- Freddi F, Mingazzi L (2022) A predictive phase-field approach for cover cracking in corroded concrete elements. *Theor Appl Fract Mech* 122:103657
- Fang X, Pan Z, Chen A (2022) Phase field modeling of concrete cracking for non-uniform corrosion of rebar. *Theor Appl Fract Mech* 121:103517
- Frémond M (1985) Dissipation dans l'adhérence des solides. *C R Acad Sci Paris Sér II* 300:709–714
- Hilber HM, Hughes TJR, Taylor RL (1977) Improved numerical dissipation for time integration algorithms in structural dynamics. *Earthq Eng Struct Dyn* 5(3):283–292
- Kružík M, Roubíček T (2019) Mathematical methods in continuum mechanics of solids. *Interaction of Mech. and Math. Series*. Springer, Cham
- Kuhn C, Schlüter A, Müller R (2015) On degradation functions in phase field fracture models. *Comput Mater Sci* 108:374–384

- Luo X-L, Ye J-Y, Ma P-S, Zhang L-W (2022) Data-driven enhanced phase field models for highly accurate prediction of mode I and mode II fracture. *Comput Methods Appl Mech Eng* 400:115535
- Li Y, Yu T, Natarajan S, Bui TQ (2023) A dynamic description of material brittle failure using a hybrid phase-field model enhanced by adaptive isogeometric analysis. *Eur J Mech A* 97:104783
- Maugin GA (2015) The saga of internal variables of state in continuum thermo-mechanics. *Mech Res Commun* 69:79–86
- Molnár G, Gravouil A (2017) 2d and 3d abaqus implementation of a robust staggered phase-field solution for modeling brittle fracture. *Finite Elem Anal Des* 130:27–38
- Miehe C, Hofacker M, Welschinger F (2010) A phase field model for rate-independent crack propagation: Robust algorithmic implementation based on operator splits. *Comput Methods Appl Mech Eng* 199(45–48):2765–2778
- Mosco U (1967) A remark on a theorem of F.E. Browder. *J Math Anal Appl* 20:90–93
- Peng X, Fu Z, Zhang Z, Chen S, Ji E, Zhong Q (2023) Two different phase field models of the explicit material point method for brittle dynamic fracture. *Eng Fract Mech* 290:109449
- Raj K, Murali P (2020) Mixed mode crack propagation in staggered biocomposites using phase field modelling. *J Mech Behav Biomed Mater* 101:103421
- Roubíček T (2020) Coupled time discretization of dynamic damage models at small strains. *IMA J Numer Anal* 40(3):1772–1791
- Roubíček T, Panagiotopoulos CG (2017) Energy-conserving time discretization of abstract dynamic problems with applications in continuum mechanics of solids. *Numer Funct Anal Optim* 38(9):1143–1172
- Sargado JM, Keilegavlen E, Berre I, Nordbotten JM (2018) High-accuracy phase-field models for brittle fracture based on a new family of degradation functions. *J Mech Phys Solids* 111:458–489
- Tanné E, Li T, Bourdin B, Marigo J-J, Maurini C (2018) Crack nucleation in variational phase-field models of brittle fracture. *J Mech Phys Solids* 110:80–99
- Vodička R, Mantič V, Roubíček T (2014) Energetic versus maximally-dissipative local solutions of a quasi-static rate-independent mixed-mode delamination model. *Meccanica* 49(12):2933–296
- Vodička R (2016) A quasi-static interface damage model with cohesive cracks: SQP-SGBEM implementation. *Eng Anal Bound Elem* 62:123–140
- Vodička R (2022) A quasi-static computational model for interface and phase-field fracture in domains with inclusions. *Procedia Struct Integr* 42:927–934
- Vodička R (2023) A mixed-mode dependent interface and phase-field damage model for solids with inhomogeneities. *Theor Appl Fract Mech* 127:104009
- Vodička R (2024) A computational approach of dynamic quasi-brittle fracture using a phase-field model. *Procedia Struct Integr* 52:242–251
- Wang Q, Feng YT, Zhou W, Cheng Y, Ma G (2020) A phase-field model for mixed-mode fracture based on a unified tensile fracture criterion. *Comput Methods Appl Mech Eng* 370:113270
- Wu J-Y (2017) A unified phase-field theory for the mechanics of damage and quasi-brittle failure. *J Mech Phys Solids* 103:72–99
- Weinberg K, Wieners C (2022) Dynamic phase-field fracture with a first-order discontinuous galerkin method for elastic waves. *Comput Methods Appl Mech Eng* 389:114330
- Xu B, Xu T, Xue Y, Heap MJ, Ranjith PG, Wasantha PLP, Li Z (2022) Phase-field modeling of crack growth and interaction in rock. *Geomech Geophys Geo-Energy Geo-Resour* 8(6):180
- Yin BB, Zhang LW (2019) Phase field method for simulating the brittle fracture of fiber reinforced composites. *Eng Fract Mech* 211:321–340
- Yue Q, Zhou W, Wang Q, Feng YT, Ma G, Chang X (2022) An adaptive phase-field model based on bilinear elements for tensile-compressive-shear fracture. *Comput Math Appl* 105:112–135
- Zhang T, Hirshikesh YuT, Xing C, Natarajan S (2023) An adaptive dynamic phase-field method using the variable-node elements for cohesive dynamic fracture. *Comput Meth Appl Mech Eng* 416:116390
- Zeng Z, Ni R, Zhang X, Liu Y (2023) An explicit phase field material point method for modeling dynamic fracture problems. *Int J Numer Meth Eng*. 124(12):2680–2708
- Zhang X, Sloan SW, Vignes C, Sheng D (2017) A modification of the phase-field model for mixed mode crack propagation in rock-like materials. *Comput Methods Appl Mech Eng* 322:123–136
- Zhang P, Yao W, Hu XF, Bui TQ (2021) An explicit phase field model for progressive tensile failure of composites. *Eng Fract Mech* 241:107371

Publisher's Note Springer Nature remains neutral with regard to jurisdictional claims in published maps and institutional affiliations.